1 **TITLE**

2 Homogeneity of antibody-drug conjugates critically impacts the therapeutic efficacy in brain tumors

3

4 **AUTHORS**

5 Yasuaki Anami[1], Yoshihiro Otani[2], Wei Xiong[1], Summer Y. Y. Ha[1], Aiko Yamaguchi[1], Ningyan Zhang[1],

6 Zhiqiang An[1], Balveen Kaur[2], Kyoji Tsuchikama*[1]

7

8 [1]Texas Therapeutics Institute, The Brown Foundation Institute of Molecular Medicine, McGovern

9 Medical School, The University of Texas Health Center at Houston, Houston, Texas 77054, USA.

10 [2]Department of Neurosurgery, McGovern Medical School, The University of Texas Health Science

11 Center at Houston, Houston, Texas 77030, USA.

12 *Correspondence: Kyoji Tsuchikama (Kyoji.Tsuchikama@uth.tmc.edu)

13 **SUMMARY**

14   Glioblastoma multiforme (GBM) is characterized by aggressive growth and the poorest prognosis of

15   all brain tumor types. Most therapies rarely provide clinically meaningful improvements in outcomes of

16   patients with GBM. Antibody-drug conjugates (ADCs) are emerging chemotherapeutics with stunning

17   success in cancer management. Although promising, clinical studies of three ADCs for treating GBM,

18   including Depatux-M, have been discontinued because of safety concerns and limited therapeutic

19   benefits. Here, we report that ADC homogeneity is a critical parameter to maximize the therapeutic

20   potential in GBM therapy. We demonstrate that homogeneous conjugates generated using our linker

21   show enhanced drug delivery to intracranial brain tumors. Notably, compared to heterogeneous ADCs,

22   including a Depatux-M analog, our ADCs provide greatly improved antitumor effects and survival

23   benefits in orthotopic brain tumor models, including a patient-derived xenograft model of GBM. Our

24   findings warrant the future development of homogeneous ADCs as promising molecular entities toward

25   cures for intractable brain tumors.

26 **INTRODUCTION**

27   Glioblastoma multiforme (GBM) is the most aggressive brain tumor characterized by infiltrative

28 growth to normal tissues, high proliferation rate, abundant angiogenesis, and intratumor and inter-

29 patient heterogeneity (Inda et al., 2014; Parker et al., 2015; Shergalis et al., 2018). GBM has poorer

30 survival rates than all other brain tumors (median survival time: 15-16 months) (Chinot et al., 2014;

31 Stupp et al., 2005, 2009) due to quick relapse after standard therapy, namely surgical removal in

32 combination with radiation therapy, chemotherapy using temozolomide, and/or tumor-treating fields.

33 Deep infiltration of GBM into normal brain tissues makes complete surgical resection of tumor lesions a

34 challenging task. While surgery is a proven option for primary GBM, its clinical benefit for patients with

35 relapsed GBM remains unvalidated (Weller et al., 2014). To improve patients' survival and quality of

36 life, effective systemic therapies that can complement other treatment options are urgently needed.

37

38   Antibody-drug conjugates (ADCs) are an emerging class of chemotherapeutic agents consisting of

39 tumor-targeting monoclonal antibodies (mAbs) with highly cytotoxic payloads attached through

40 chemical linkers. ADCs can exert a durable and tumor-specific therapeutic effect by ensuring the

41 delivery of conjugated cytotoxic payloads to antigen-positive tumor cells. Eleven ADCs have been

42 approved by the U.S. Food and Drug Administration (FDA) (Dhillon, 2018; Drago et al., 2021; Mullard,

43 2021), and more than 100 ADCs are currently in clinical trials (Chau et al., 2019). Despite the success

44 in the management of other cancers, ADCs have not yet shown remarkable treatment outcomes in

45 patients with GBM. Three ADCs have advanced to clinical trials for GBM therapy: depatuxizumab

46 mafodotin (Depatux-M or ABT-414) (Phillips et al., 2016), ABBV-221 (Phillips et al., 2018), and AMG-

47 595 (Hamblett et al., 2015). These ADCs target EGFR and its active mutant EGFR variant III

48 (EGFRvIII), which are signature receptors expressed in a subset of GBM tumors (Brennan et al., 2013).

49 Unfortunately, clinical trials of the three ADCs have been terminated or discontinued (Newman, 2019;

50 Rosenthal et al., 2019; Van Den Bent et al., 2020). No survival benefit was confirmed in a Phase 3 trial

51 evaluating Depatux-M in patients with newly diagnosed GBM (Van Den Bent et al., 2020). In a

3

52   preclinical study, ABBV-221 demonstrated greater treatment efficacy than could be achieved with

53   Depatux-M; however, a Phase 1 study has raised safety concerns (Newman, 2019). The development

54   of AMG-595 was discontinued upon completion of a Phase 1 study due to limited efficacy. Unlike other

55   solid tumors, efficient mAb delivery to the brain is particularly challenging because of the blood–brain

56   barrier (BBB), a tightly constituted endothelial cell border restricting the influx of large molecules from

57   the vasculature to the brain parenchyma (Abbott et al., 2010; Banks, 2016). Therefore, to establish

58   ADC-based GBM therapy as a practical clinical option, identifying and optimizing molecular parameters

59   that negatively influence BBB permeability, therapeutic efficacy, and safety profiles are critically

60   important.

61

62   Herein, we report that ADC homogeneity plays a critical role in payload delivery to intracranial brain

63   tumors. We demonstrate that homogeneous ADCs elicit improved antitumor activity in intracranial brain

64   tumor-bearing mouse models compared with heterogeneous variants prepared by stochastic cysteine–

65   maleimide or lysine–amide coupling. We also show using mouse models how homogeneous

66   conjugation at an optimal drug-to-antibody ratio (DAR) improves efficiency in payload delivery to

67   intracranial GBM tumors, leading to dramatically extended survival. This finding suggests that ensuring

68   ADC homogeneity is a crucial step to achieving clinically meaningful treatment outcomes in brain

69   tumors, including GBM.

70

71   **RESULTS**

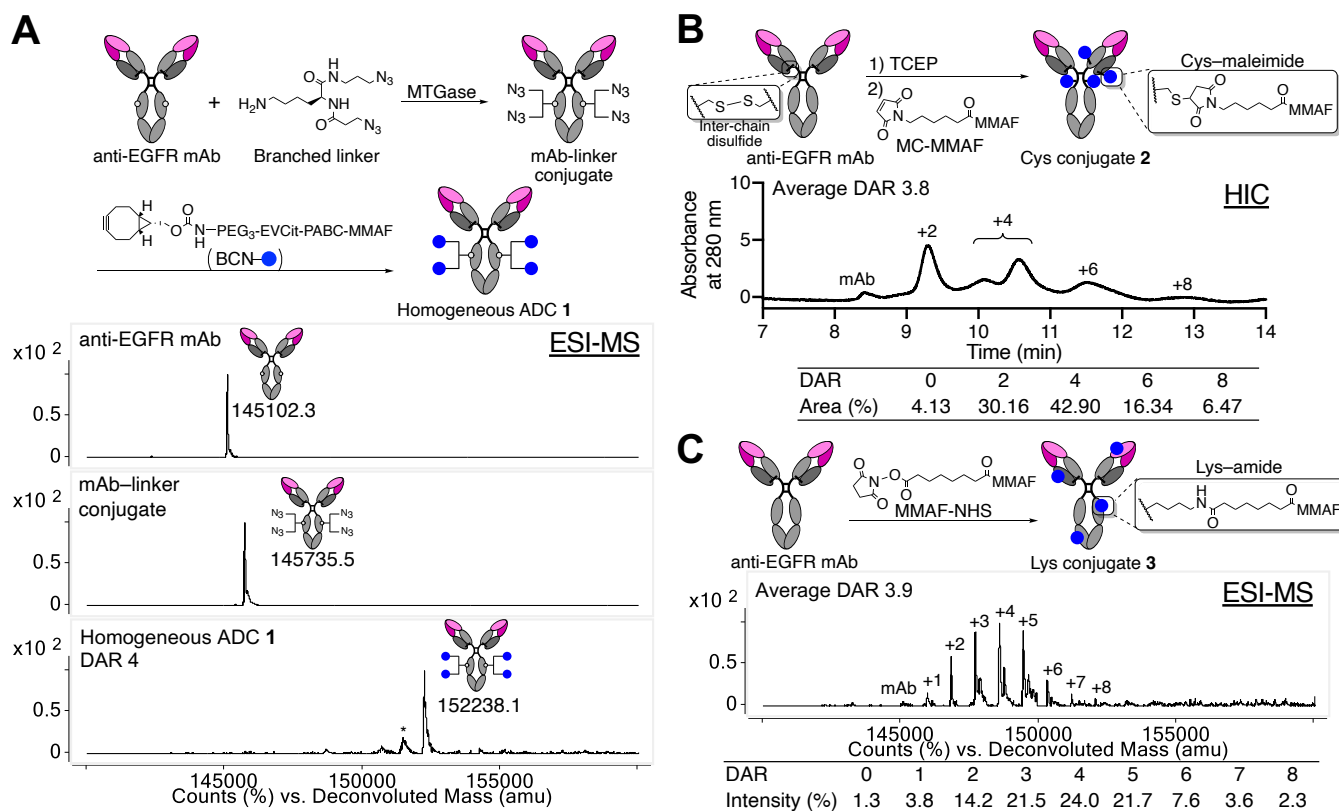72   **Construction of anti-EGFR ADCs with varied homogeneity**

73   We have previously established click chemistry-empowered branched linkers for installing two

74   identical or different payloads onto a single antibody in a site-specific and quantitative manner (Anami

75   and Tsuchikama, 2020; Anami et al., 2017; Yamazaki et al., 2021). We have also developed the

76   glutamic acid–valine–citrulline (EVCit) cleavable linker enabling the intracellular release of payloads in

77   a traceless fashion while minimizing premature linker degradation in human and mouse plasma (Anami

4

78   et al., 2018). Indeed, we have confirmed that the maximum tolerated dose of an EVCit-based dual-drug

79   ADC containing monomethyl auristatin E (MMAE) and monomethyl auristatin F (MMAF) is higher than

80   40 mg/kg in non-tumor bearing mice (Yamazaki et al., 2021). Using these technologies, we set out to

81   construct a homogeneous ADC targeting both EGFR and EGFRvIII (**Figure 1A**). We used cetuximab

82   with N88A and N297A double mutations for ADC construction. Cetuximab, a human–murine chimeric

83   mAb targeting the extracellular domain III of EGFR and EGFRvIII, has been approved for the treatment

84   of colorectal cancer and head and neck cancer (EliLilly, 2004). The N88A/N297A double mutations

85   remove two *N*-glycans on the side chains of asparagine 88 within the Fab moiety and asparagine 297

86   within the Fc moiety (Giddens et al., 2018). Thus, this modification allows the omission of the

87   deglycosylation step required for following microbial transglutaminase (MTGase)-mediated linker

88   conjugation. In addition, *N*-glycan removal abrogates immune responses derived from interactions with

89   Fcγ receptors expressed in immune cells, which can minimize undesired systemic toxicity or

90   inflammatory response (Herbst et al., 2020; White et al., 2020). Atezolizumab (TECENTRIQ®, anti-PD-

91   L1 mAb) is a recent example with an N297A mutation approved by the FDA.

92

93   We began the ADC construction by installing branched diazide linkers site-specifically onto

94   glutamine 295 (Q295) within the parent N88A/N297A anti-EGFR mAb using MTGase (Anami and

95   Tsuchikama, 2020) (**Figure 1A**). This enzymatic conjugation yielded a homogeneous mAb–branched

96   linker conjugate in high yield. In parallel, we synthesized a payload module consisting of

97   bicyclo[6.1.0]nonyne (BCN, as a reaction handle for following strain-promoted azide–alkyne click

98   reaction), EVCit (as a cathepsin-responsive cleavable sequence), *p*-aminobenzyloxycarbonyl (PABC)

99   spacer, and MMAF (BCN–EVCit–PABC–MMAF, see Supplementary Information for synthesis details).

100   Finally, the click reaction between the azide groups on the branched linkers and BCN–EVCit–PABC–

101   MMAF quantitatively afforded anti-EGFR ADC **1** with a DAR of 4. We confirmed the homogeneity of

102   ADC **1** by reverse-phase HPLC and electrospray ionization mass spectrometry (ESI-MS) analysis

103   (**Figure S1A**). Using the same parent anti-EGFR mAb, we also prepared two heterogeneous variants

5

104   that resemble the structure of Depatux-M (Cys conjugate **2**) (Phillips et al., 2016) or the conjugation

105   modality of AMG-595 (Lys conjugate **3**) (Hamblett et al., 2015). For the preparation of Cys conjugate **2**,

106   non-cleavable maleimidocaproyl MMAF (MC–MMAF) was installed by partial disulfide bond reduction

107   and following cysteine–maleimide alkylation. We confirmed by hydrophobic interaction chromatography

108   (HIC) analysis that Cys conjugate **2** consisted of DAR-0, 2, 4, 6, and 8 species (average DAR: 3.8,

109   **Figure 1B**). To prepare Lys conjugate **3**, we synthesized and used non-cleavable MMAF–*N*-

110   hydroxysuccinimide (NHS) ester for lysine coupling-based conjugation (See Supplementary Information

111   for synthesis details). ESI-MS analysis revealed that this heterogeneous conjugate consisted of multiple

112   products with DARs ranging from 0 to 8 (average DAR: 3.9, **Figure 1C**).

113

115   **Figure 1.** Construction and characterization of anti-EGFR ADCs. **A** Preparation and ESI-MS analysis of

116   homogeneous ADC **1**. Top panel: N88A/N297A anti-EGFR mAb (cetuximab mutant). Middle panel:

117   mAb–linker conjugate. Bottom panel: homogeneous ADC **1** with a DAR of 4. Asterisk (*) indicates a

118   fragment ion detected in ESI-MS analysis. **B** Preparation and HIC analysis of Cys conjugate **2** under

119   physiological conditions (phosphate buffer, pH 7.4). The average DAR was determined to be 3.8 based

120   on UV peak area of each DAR species. **C** Preparation and ESI-MS analysis of Lys conjugate **3**. The

121   average DAR was determined to be 3.9 based on the ion intensity of each DAR species. BCN,

122   bicyclo[6.1.0]nonyne; DAR, drug-to-antibody ratio; ESI-MS, electrospray ionization mass spectrometry;

123   MC, maleimidecaproyl; MMAF, monomethyl auristatin F; MTGase, microbial transglutaminase; HIC,

124   hydrophobicity interaction chromatography; NHS, *N*-hydroxysuccinimide; PABC, *p*-

125   aminobenzyloxycarbonyl; PEG, polyethylene glycol; TCEP, tris(2-carboxyethyl)phosphine.

126

127   **Cysteine–maleimide conjugation does not impair EGFR-specific potency *in vitro* but reduces**

128   **long-term stability**

129   Size-exclusion chromatography (SEC) analysis revealed that all ADCs generated predominantly

130   existed in the monomer form (**Figure S1B**). These ADCs were also tested for long-term stability under

131   physiological conditions by being incubated at 37 °C in PBS (pH 7.4) for 28 days. We observed no

132   significant degradation or aggregation for homogeneous ADC **1** and Lys conjugate **3** (**Figure S2**). In

133   contrast, Cys conjugate **2** showed two new peaks after the peak corresponding to its monomeric form,

134   indicating that fragmentation or partial dissociation of the heavy and light chains occurred. These

135   results suggest that both MTGase-mediated homogeneous conjugation and lysine coupling offer higher

136   thermal stability compared to the one achieved by cysteine–maleimide conjugation.

137

138   Next, we assessed antigen-specific binding of the ADCs by cell-based ELISA (**Figure 2A** and Table

139   **S1**). All ADCs showed binding affinities for EGFRvIII-positive U87ΔEGFR-luc cells (K_D: 0.044–0.047

140   nM) comparable to that of the unmodified N88A/N297A cetuximab (K_D: 0.039 nM). In addition, none of

141   the ADCs bound to EGFR-negative HEK293 cells. These results demonstrate that the ADCs retained

142   their binding affinity and specificity regardless of conjugation methods. We also tested these conjugates

143   for cell killing potency in U87ΔEGFR-luc, Gli36δEGFR (EGFRvIII-positive), and HEK293 cells (EGFR-

144   negative control) (**Figure 2B** and **Table S2**). All DAR 4 ADCs showed comparable potency in the

145   EGFRvIII-positive GBM cells (EC_{50} values: 0.072–0.140 nM in U87ΔEGFR-luc and 0.035–0.048 nM in

146   Gli36δEGFR cells), but not in HEK293 cells. This result is in line with previous reports demonstrating

7

147   that MMAF ADCs can exert pM-level cell killing potency with or without a cleavable linker (Deonarain et

148   al., 2014; Doronina et al., 2006).
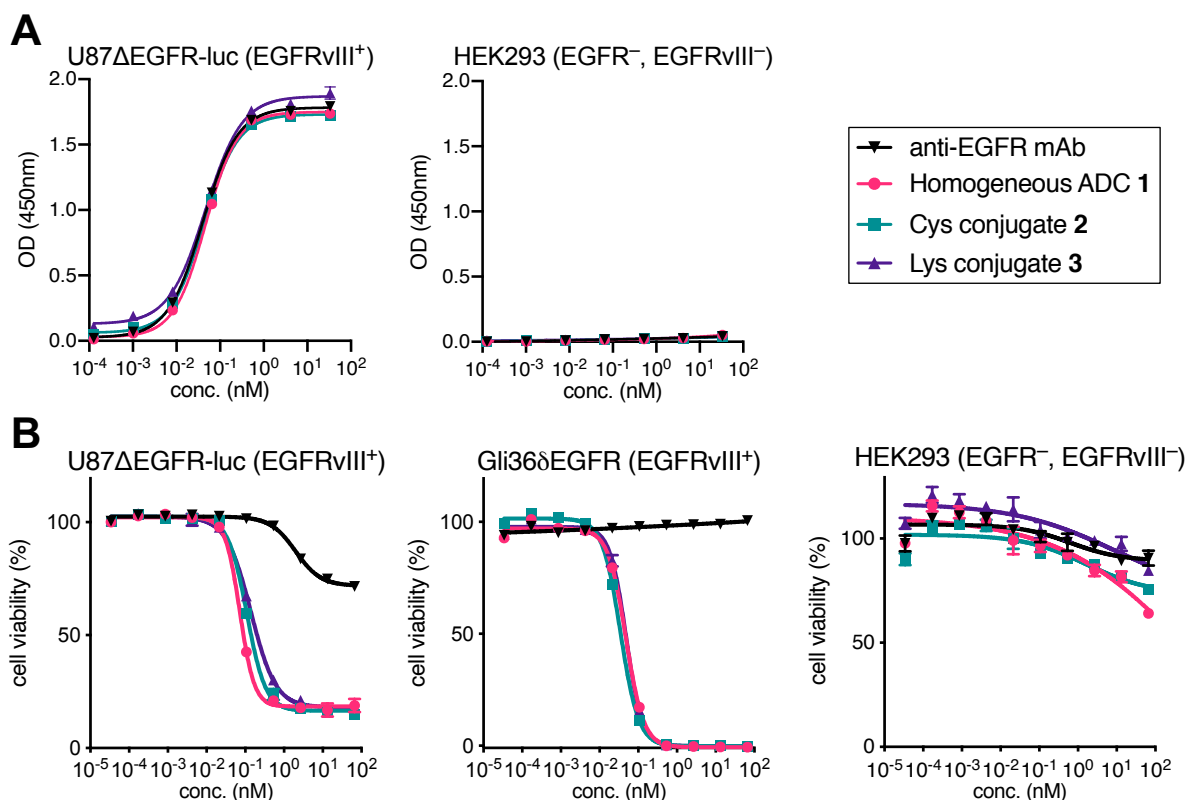
Figure 2. Evaluation of antigen-specific binding and *in vitro* cytotoxicity. **A** Cell-based ELISA in U87ΔEGFR-luc (EGFRvIII$^+$) and HEK293 (wtEGFR$^-$, EGFRvIII$^-$) cells. **B** Cell killing potency in U87ΔEGFR-luc, Gli36δEGFR (EGFRvIII$^+$), and HEK293. We tested the parent anti-EGFR mAb (black inversed triangle), homogeneous ADC **1** (magenta circle), Cys conjugate **2** (green square), and Lys conjugate **3** (purple triangle). Concentrations are based on the antibody dose without normalizing to each DAR. All assays were performed in triplicate. Data are presented as mean values ± SEM.

The homogeneous anti-EGFR ADC exerts significantly improved therapeutic efficacy in orthotopic mouse models of GBM

159   To evaluate the *in vivo* anti-tumor activity of the three anti-EGFR ADCs, we first performed a

160   treatment study using a cell line-derived xenograft model of human GBM. To gain clinically translatable

161   insights into the influence of conjugation modality on drug delivery to brain tumors, intracranially

162   implanted models were used instead of subcutaneous models. NOD*scid* gamma (NSG) mice were

8

163   orthotopically implanted with U87ΔEGFR-luc cells and injected intravenously with a single dose of each

164   ADC (homogeneous ADC **1**, Cys conjugate **2**, or Lys conjugate **3**) at 3 mg/kg 5 days post-implantation

165   (**Figure 3A**). Tumor growth and body weight were monitored periodically (**Figure S3**). No acute toxicity

166   associated with ADC administration was observed in either group over the course of the study (**Figure**

167   **S3A**). The short survival time observed for the untreated group (median survival: 14 days, **Figure 3B**)

168   demonstrates the extremely aggressive growth of this GBM model. Homogeneous ADC **1** exerted

169   remarkable antitumor activity with statistically significant survival benefits; the median survival rate

170   increased from 14 days in the untreated group to 43 days in the treated cohort (207% extension, P =

171   0.0032). In addition, two out of six mice survived at the end of the study (Day 60) with no detectable

172   bioluminescence signal from implanted tumors (**Figure S3B**), indicating that these two mice achieved

173   complete remission. In contrast, the heterogeneous conjugates exhibited limited therapeutic effects with

174   marginally increased median survival times (22 days, Cys conjugate **2** and 23.5 days, Lys conjugate **3**),

175   which were inferior to that provided by homogeneous ADC **1** (P = 0.0046). Indeed, all mice in these two

176   groups died or reached the pre-defined humane endpoint by the end of the study (**Figure 3B**). This

177   result is in contrast to our observation that ADCs **1**–**3** showed comparable *in vitro* cell killing potency in

178   U87ΔEGFR-luc cells (**Figure 2B**).

179

180   To further validate the therapeutic potential of homogeneous ADC **1,** we sought to use a patient-

181   derived xenograft (PDX) tumor model of GBM. PDX models maintain pathohistological and genetic

182   properties of original tumors as well as therapeutic responses to anti-cancer treatments. As such, PDX

183   models provide clinically relevant and translatable data (Hidalgo et al., 2014). To this end, we used

184   GBM12, a PDX model of GBM overexpressing wild-type EGFR (Sarkaria et al., 2006). A study has

185   shown that GBM12 tumors show heterogeneous BBB disruption, meaning that some GBM12 tumor

186   cells are likely protected by an intact BBB (Parrish et al., 2015). Before initiating an *in vivo* assessment,

187   homogeneous ADC **1** and heterogeneous Cys conjugate **2** were evaluated for cell killing potency in

188   GBM12 cells. Both ADCs efficiently killed GBM12 cells with comparable EC_{50} values (homogeneous

189 ADC **1**: 0.08 nM, Cys conjugate **2**: 0.11 nM, **Figure S4A**). Next, we investigated whether or not

190 homogeneous conjugate **1** also showed a greater treatment effect in the orthotopic GBM12 mouse

191 model than could be achieved by Cys conjugate **2**. NSG mice bearing intracranial GBM12 tumors were

192 injected intravenously with a single dose of either conjugate (3 mg/kg) 8 days post-implantation (**Figure**

193 **3C**). Tumor size was noninvasively measured by magnetic resonance imaging (MRI) on Day 18. No

194 acute toxicity was observed in either group over the course of the study (**Figure S4B**). Homogeneous

195 ADC **1** effectively suppressed tumor growth with a statistically significant survival benefit (median

196 survival: 31 days, +55% relative to the vehicle group, $P = 6.8 \times 10^{-8}$), whereas Cys conjugate **2** showed

197 a marginal therapeutic effect (median survival: 23 days, +15% extension, $P = 0.12$, **Figure 3D**). MRI on

198 Day 18 showed that the tumors treated with homogeneous ADC **1** (average size: 14.71 ± 7.90 mm^3)

199 were markedly smaller than the untreated ones (average size: 203.46 ± 23.81 mm^3, $P < 0.0001$,

200 **Figures 3E** and **3F**). Cys conjugate **2** also inhibited tumor growth (average size: 88.63 ± 13.71 mm^3)

201 but less effectively than homogeneous ADC **1** ($P = 0.0279$). To investigate how each ADC influenced

202 cell proliferation and apoptosis, we performed immunohistochemistry analysis of brain tissues

203 harvested from each group at the terminal stage (vehicle: 20–26 days, ADC **1**: 30–35 days; Cys

204 conjugate **2**: 24–31 days, **Figures S4C–F**). About 80% of cells were Ki67-positive in the vehicle-treated

205 group, while about 70% of cells were Ki67-positive in both ADC-treated groups (**Figure 3G**). This result

206 indicates that antiproliferative effects by both ADCs declined to similar levels at the terminal stage. In

207 contrast, the population of cleaved caspase-3 (cCaspase-3)-positive cells in the tumors treated with

208 ADC **1** ($9.4 \pm 2.8\%$) was significantly higher than that in the tumors treated with vehicle ($1.1 \pm 0.1\%$, $P =$

209 0.0064) or Cys conjugate **2** ($2.8 \pm 0.6\%$, $P = 0.0333$, **Figure 3H**), suggesting that homogeneous ADC **1**

210 induced apoptosis more effectively than heterogeneous ADC **2** over the course of the study. Given that

211 the histopathology analysis was performed at the terminal stage of each group, more significant

212 differences in Ki67 and cCaspase-3 levels could have been observed at the same time point in the

213 early stage. Collectively, these results demonstrate that homogeneous ADC **1** can eradicate intracranial

214 GBM tumors more efficiently than its heterogeneous variants.

10
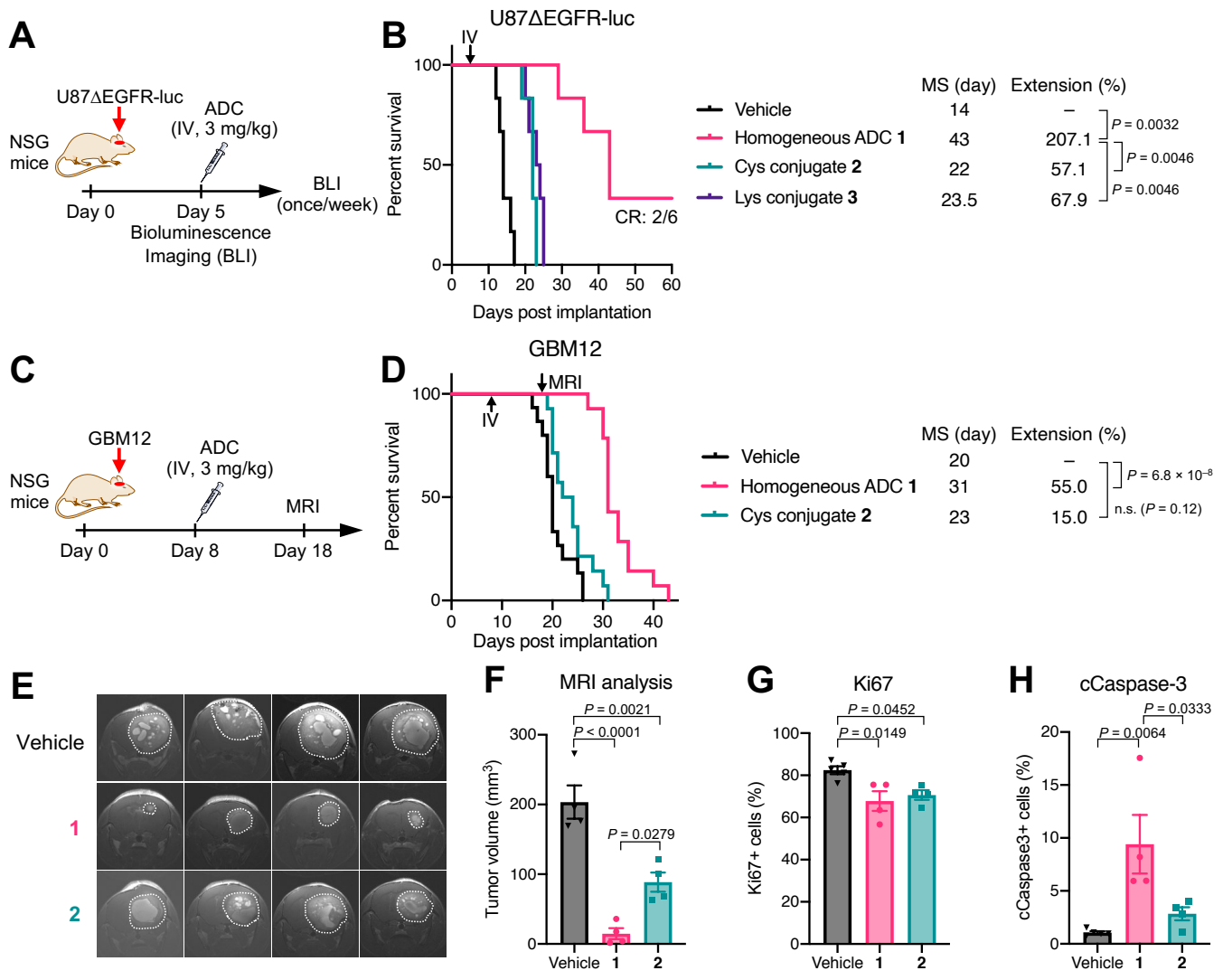
Figure 3. ADC homogeneity enhances therapeutic efficacy in orthotopic GBM mouse models. **A** Study schedule in the U87ΔEGFR-luc xenograft model. Male and female NSG mice were intracranially implanted with U87ΔEGFR-luc cells. Five days after tumor implantation, each group was treated with a single intravenous administration of each ADC at 3 mg/kg and monitored by BLI once a week. **B** Survival curves in the U87ΔEGFR-luc model (n = 6/group). Vehicle (black), homogeneous ADC **1** (magenta), Cys conjugate **2** (green), and Lys conjugate **3** (purple). Two out of six mice treated with homogeneous ADC **1** survived over 60 days without detectable tumor-derived bioluminescence signal. All animals other than the ones that were found dead or achieved complete remission were euthanized at the pre-defined humane endpoint, which were counted as deaths. **C** Study schedule in the GBM12 PDX model. Tumor-bearing NSG mice were treated with ADC **1** or **2** at 3 mg/kg 8 days post-implantation. MRI was performed on Day 18. **D** Survival curves in the GBM12 model (n = 15 for vehicle; n = 14 for ADCs). **E** Coronal MRI images on Day 18 (n = 4). Tumor lesions are indicated with white dots. **F** Estimated tumor volume by MRI image-based quantification (n = 4). **G** Population of Ki67-

11

229 positive cells in the GBM12 tumors harvested at the terminal stage (n = 5 for vehicle, n = 4 for ADCs).

230 **H** Population of cCaspase-3-positive cells in the GBM12 tumors harvested at the terminal stage (n = 5

231 for vehicle, n = 4 for ADCs). Data are presented as mean values ± SEM. Kaplan-Meier survival curve

232 statistics were analyzed with a log-rank test. To control the family-wise error rate in multiple

233 comparisons, crude *P* values were adjusted by the Bonferroni method. For MRI and tissue analysis, a

234 one-way ANOVA with a Tukey-Kramer post hoc test was used (see **Table S4** for details). BLI,

235 bioluminescence imaging; cCaspase-3, cleaved caspase-3; CR, complete remission; MRI, magnetic

236 resonance imaging; MS, median survival; PDX, patient-derived xenograft.

237

238 **Homogeneity also improves *in vivo* therapeutic efficacy of other ADCs for EGFRvIII- and HER2-**

239 **positive brain tumors**

240 To generalize our findings, we tested other homogeneous ADCs for treatment efficacy in orthotopic

241 brain tumor models. To this end, homogeneous anti-EGFRvIII ADC **4** (DAR 4) and heterogeneous

242 variant **5** (Lys conjugate, average DAR: 4.7) were constructed from N297A depatuxizumab, the parent

243 mAb of Depatux-M (Phillips et al., 2016) (**Figure S5A**). Both ADCs showed comparable cell killing

244 potency in EGFRvIII-positive U87ΔEGFR-luc cells (EC$_{50}$ values: 0.15 nM, homogeneous ADC **4** and

245 0.26 nM, Lys conjugate **5**, **Figure S5B**). Subsequently, NSG mice bearing intracranial U87ΔEGFR-luc

246 tumors were treated with a single dose of each ADC at 3 mg/kg 5 days after tumor implantation (**Figure**

247 **4A**). Homogeneous ADC **4** showed a remarkable survival benefit (median survival: >60 days). Four out

248 of six mice treated with homogeneous ADC **4** survived over the course of the study. In addition, MRI on

249 Day 61 showed no detectable brain tumor lesion in these survivors, indicating complete remission

250 (**Figure S5C**). In contrast, heterogeneous variant **5** extended median survival time (33 days) less

251 significantly than homogeneous ADC **4** (*P* = 0.0195, **Figure 4B**).

252

12
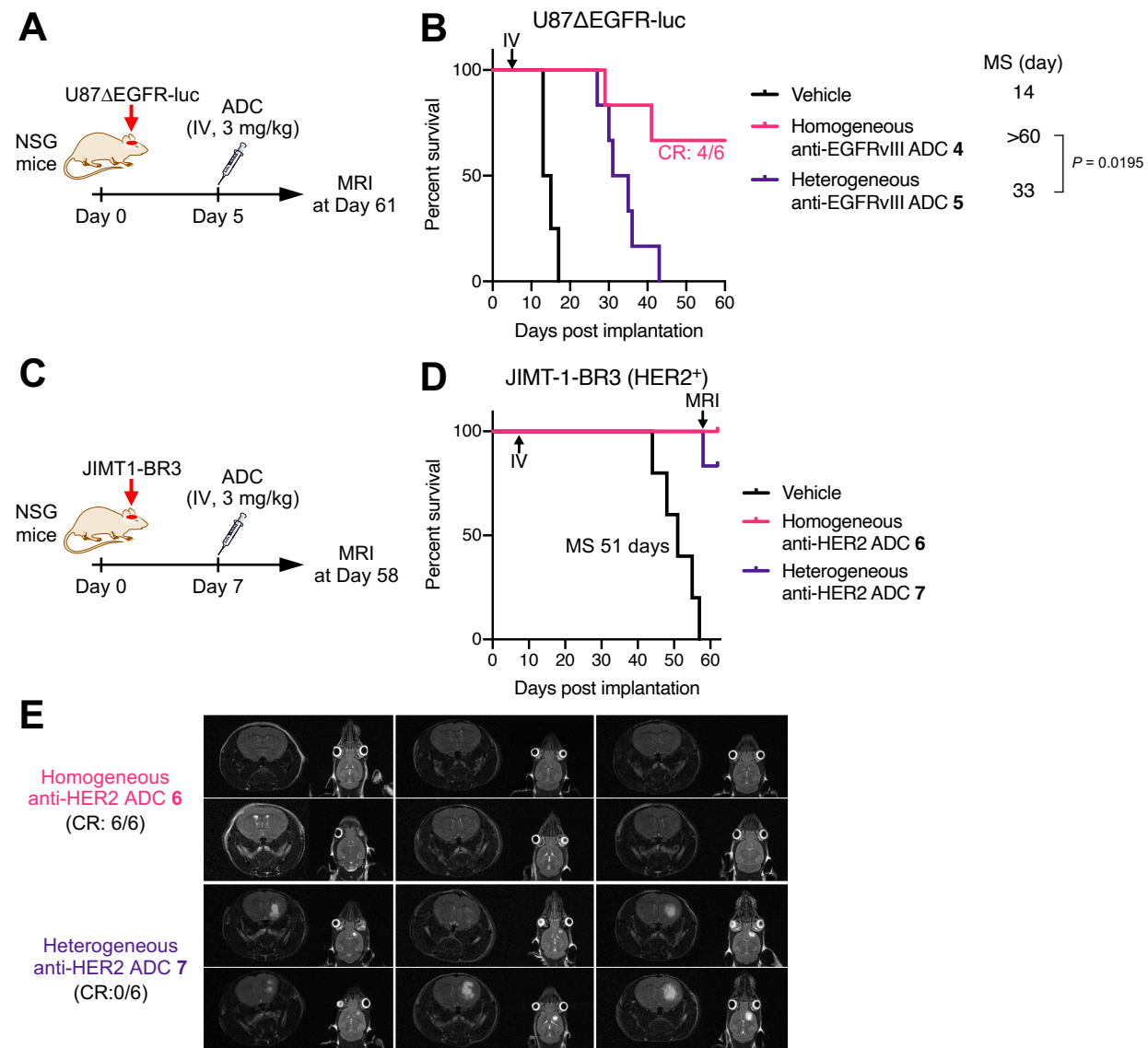
Figure 4. Homogeneous depatuxizumab- and trastuzumab-based ADCs show enhanced therapeutic efficacy in orthotopic brain tumor mouse models. **A** Study schedule in the orthotopic U87ΔEGFR-luc xenograft mouse model. Male and female NSG mice were intracranially implanted with U87ΔEGFR-luc cells. Five days after tumor implantation, each group was treated with a single intravenous administration of each depatuxizumab-based anti-EGFRvIII ADC at 3 mg/kg. MRI was performed on Day 61. **B** Survival curves in the U87ΔEGFR-luc model. Vehicle (black, n = 4), homogeneous ADC **4** (magenta, n = 6), and heterogeneous Lys conjugate **5** (purple, n = 6). Four out of six mice treated with homogeneous ADC **4** survived over 60 days without detectable tumor lesions (**Figure S5C**). All animals other than the ones that were found dead or achieved complete remission were euthanized at the pre-defined humane endpoint, which were counted as deaths. **C** Study schedule for the intracranially implanted JIMT1-BR3 tumor mouse model. NSG mice bearing intracranial JIMT-1-BR3 tumors were

13

265 injected intravenously with a single dose of each trastuzumab-based anti-HER2 ADC at 3 mg/kg 7 days

266 post-implantation. MRI was performed on Day 58. **D** Survival curves in the JIMT-1-BR3 model (n = 6).

267 Vehicle (black), homogeneous anti-HER2 ADC **6** (magenta), and heterogeneous Lys conjugate **7**

268 (purple). **E** Coronal and sagittal MRI images of the intracranial JIMT-1-BR3 tumor-bearing mice on Day

269 58. Brain tumor lesions were detected in the mice treated with heterogeneous ADC **7** (CR: 0/6) but not

270 in those treated with homogeneous ADC **6** (CR: 6/6). Kaplan-Meier survival curve statistics were

271 analyzed with a log-rank test (see **Table S4** for details).

272

273   Next, we performed similar *in vitro* and *in vivo* studies using a HER2-positive brain tumor model.

274 Brain metastasis is observed in 25–50% patients with advanced HER2-positive breast tumors (Zimmer

275 et al., 2020), representing a difficult-to-treat population. We prepared anti-HER2 homogeneous ADC **6**

276 (DAR 4) and a heterogeneous variant (Lys conjugate **7**, average DAR: 4.2) from N297A trastuzumab

277 and evaluated their cell killing potency in HER2-positive JIMT-1-BR3 cells (**Figures S6A** and **S6B**).

278 JIMT-1-BR3 is a HER2-positive breast cancer cell line established from a subpopulation of the parent

279 JIMT-1 cells that metastasized to the brain in a rodent model (Palmieri et al., 2014). Both ADCs

280 efficiently killed JIMT-1-BR3 cells with comparable EC_{50} values (homogeneous ADC **6**: 0.037 nM, Lys-

281 conjugate **7**: 0.059 nM, **Figure S6B**). Subsequently, NSG mice bearing intracranial JIMT-1-BR3 tumors

282 were injected intravenously with each ADC at 3 mg/kg 7 days post tumor implantation (**Figure 4C**).

283 Most mice in both ADC groups survived over the course of the study (Homogeneous ADC **4**: all mice,

284 heterogeneous ADC **5**: 5 out of 6 mice), while the median survival time without treatment was 51 days

285 (**Figure 4D**). However, MRI on Day 58 revealed a clear difference in efficacy between these two ADC

286 groups; tumor lesions were detected in all mice treated with heterogeneous ADC **7** but not in those

287 treated with homogeneous ADC **6** (**Figure 4E**). Hematoxylin and eosin (H&E) staining of the brain

288 tissues also validated this observation (**Figure S6C**). Collectively, these findings strongly support our

289 hypothesis that the use of homogeneous ADCs can lead to significantly improved treatment outcomes

290 in a broad range of brain tumors compared to heterogeneous ADC-based treatment.

291

14

292 **Clearance and linker stability in circulation are not the primary factors reducing the efficiency in**

293 **payload delivery to brain tumors**

294   To understand how the antibody–drug conjugation modality impacts overall efficacy in the treatment

295 of brain tumors, we set out to assess *in vivo* pharmacokinetic (PK) profiles of selected ADCs.

296 Homogeneous anti-EGFR ADC **1**, heterogeneous Cys conjugate **2**, heterogeneous Lys conjugate **3**, or

297 the parental anti-EGFR mAb (3 mg/kg) was intravenously administered into CD-1 mice$^{®}$. Subsequently,

298 blood samples were periodically collected. The concentrations of both total mAb and intact ADC were

299 then determined by sandwich ELISA. In total mAb analysis, homogeneous ADC **1** and Lys conjugate **3**

300 showed half-lives at the elimination phase ($t_{1/2\beta}$ = 9.8 days, ADC **1** and $t_{1/2\beta}$ = 10.4 days, Lys conjugate

301 **3**) comparable with that of the unmodified mAb (10.9 days), whereas Cys conjugate **2** showed a slightly

302 decreased half-life ($t_{1/2\beta}$ = 7.8 days, **Figure 5A** and **Table S3**). We found that Cys conjugate **2** showed

303 thermal instability after a 28-day incubation under physiological conditions probably due to partly

304 cleaved interchain disulfide bonds (**Figure S2C**). This instability may account for the increased

305 clearance rate. In intact ADC analysis, no significant decrease in half-lives was observed for

306 homogeneous ADC **1** ($t_{1/2\beta}$ = 8.6 days) or Lys conjugate **3** ($t_{1/2\beta}$ = 8.9 days), indicating that there was

307 almost no premature release of MMAF during circulation (**Figure 5B** and **Table S3**). In contrast, the

308 concentration of intact Cys conjugate **2** declined at a faster rate ($t_{1/2\beta}$ = 4.2 days), indicating that the

309 conjugated MMAF was partly lost in circulation. Previous reports have shown that cysteine-containing

310 serum proteins such as albumin promote dissociation of cysteine–maleimide linkage within ADCs

311 through a thiol exchange reaction, leading to partial deconjugation of payloads in circulation (Lyon et

312 al., 2014; Tumey et al., 2014).
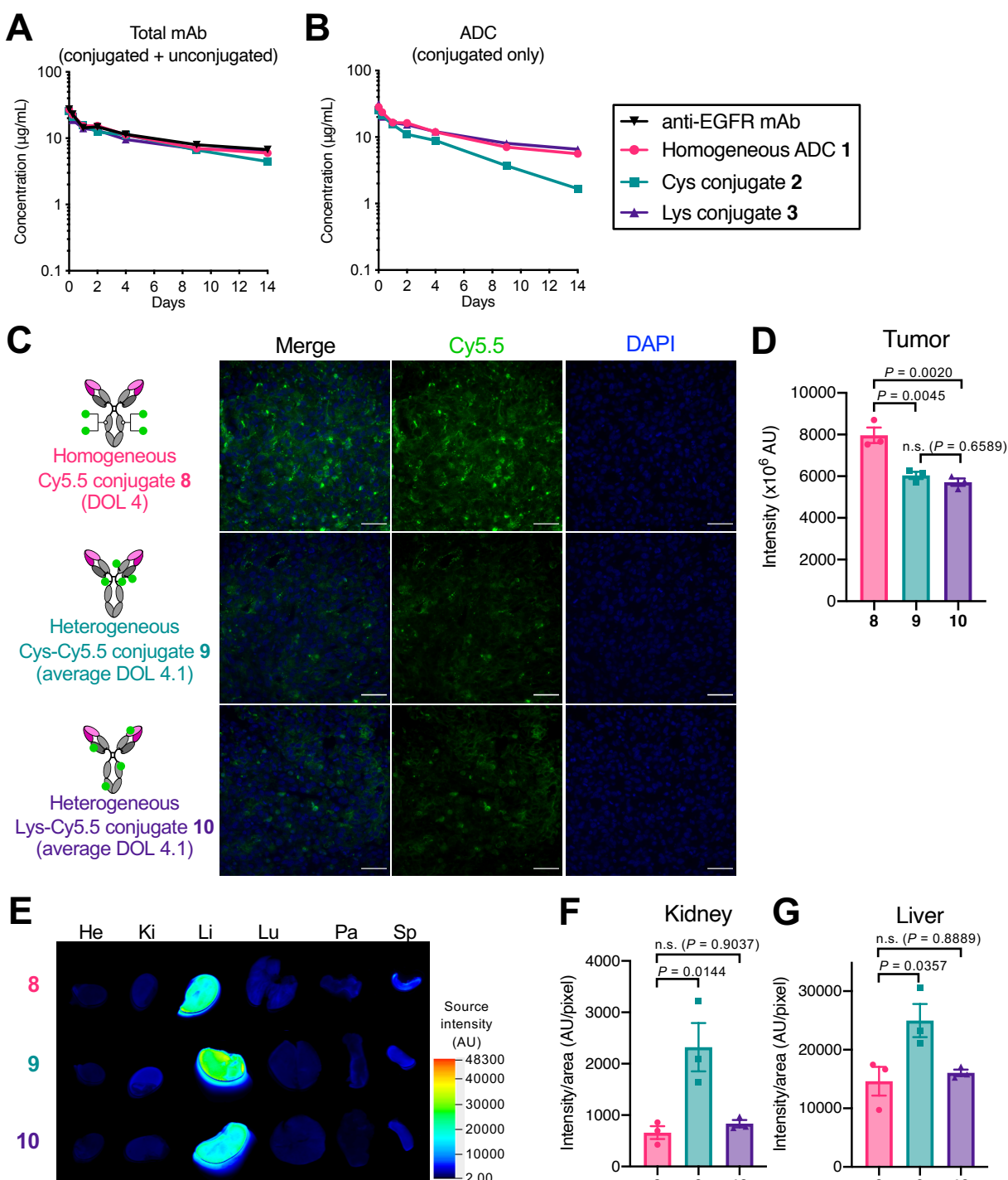
313

15

Figure 5. Promoted clearance and premature payload loss in circulation are not the primary factors attenuating the brain tumor-targeting efficiency of ADCs. **A,B** PK of unmodified N88A/N297A anti-EGFR mAb (black inversed triangle), homogeneous ADC **1** (magenta circle), Cys conjugate **2** (green square), and Lys conjugate **3** (purple triangle) in female CD-1® mice (n = 3). At the indicated time points, blood was collected to quantify total antibody (conjugated and unconjugated, **A**) and intact ADC (conjugated only, **B**) by sandwich ELISA. **C** Fluorescence images of brain tumor tissues harvested 48

321 hours after injecting each Cy5.5 conjugate (n = 3, scale bar: 50 μm). **D** Semi-quantification of the Cy5.5

322 signal detected in the brain tumor tissues. Three regions of interest (ROI) were randomly selected in

323 each tissue sample to calculate signal intensity. **E** Ex vivo fluorescence images of the other organs (He,

324 heart; Ki, kidney; Li, liver; Lu, lung; Pa, pancreas; Sp, spleen) detected using a 700 nm channel (n = 3).

325 **F,G** Semi-quantification of the Cy5.5 signal detected in the kidneys and liver. A representative image

326 from each group is shown in all panels of fluorescence images. Data are presented as mean values ±

327 SEM. For statistical analysis, a one-way ANOVA with a Tukey-Kramer post hoc test was used (see

328 **Table S4** for details). DOL, degree of labeling.

329

330   As demonstrated above, promoted clearance and payload deconjugation may partly account for the

331 poor treatment efficacy observed for Cys conjugate **2** in the orthotopic GBM models. However, these

332 factors are likely irrelevant to the inferior efficacy observed for the lysine conjugates, which were

333 designed not to show thermal instability or undergo deconjugation in circulation. To uncover other

334 contributing factors, we performed a biodistribution study using the orthotopic U87ΔEGFR-luc xenograft

335 mouse model. As surrogates of the ADCs we used earlier, the following fluorescent dye conjugates

336 were prepared from the N88A/N297A cetuximab: homogeneous Cy5.5 conjugate **8** (degree of labeling

337 or DOL: 4) and two heterogeneous Cy5.5 conjugates by cysteine–maleimide coupling (Cys-Cy5.5

338 conjugate **9**, average DOL: 4.1) and lysine coupling (Lys-Cy5.5 conjugate **10**, average DOL: 4.1,

339 **Figures S7A–C**). We synthesized and used DBCO–EVCit–Cy5.5 module to construct homogeneous

340 conjugate **8** (see Supplementary Information for synthesis details). In all cases, Cy5.5 was incorporated

341 as a payload surrogate into the parent mAb with the same linkers and conjugation chemistries that

342 were used to prepare corresponding ADCs. Orthotopic U87ΔEGFR-luc tumor-bearing NSG mice were

343 administered intravenously with each dye conjugate at 3 mg/kg 5 days post tumor implantation. Two

344 days after administration, all animals underwent cardiac perfusion for removing conjugates circulating

345 or bound to the vascular endothelial cells. We then harvested major organs including tumor-bearing

346 brains. Fluorescence imaging revealed that homogeneous Cy5.5 conjugate **8** accumulated in the brain

347 tumors more effectively than heterogeneous conjugates **9** (P = 0.0045) and **10** (P = 0.0020, **Figures 5C**

348 and **5D**). We did not see a significant difference in intracranial U87ΔEGFR-luc tumor targeting ability

349 between Cys conjugate **9** and Lys conjugate **10**. We also confirmed in a separate biodistribution study

350 that the cathepsin-responsive cleavage EVCit linker did not significantly contribute to the enhanced

351 accumulation in U87ΔEGFR-luc tumors (**Figures S7D and S7E**). Cys-Cy5.5 conjugate **9** showed an

352 increased fluorescent signal in the kidneys and liver compared to homogeneous Cy5.5 conjugate **8**

353 (kidneys: P = 0.0144, liver: P = 0.0357), due probably to partial deconjugation of the maleimide-Cy5.5

354 modules in circulation and following hepatic and renal clearance (**Figures 5E–G**). However, we did not

355 observe such increased liver and kidney accumulation for Lys-Cy5.5 conjugate **10**. Taken together,

356 these findings suggest that promoted clearance of conjugated payloads and linker instability are not the

357 primary factors attenuating the brain tumor-targeting efficiency.

358

359 **Homogeneous conjugation enables efficient payload delivery to intracranial tumors for days**

360   We performed longitudinal intravital imaging to clarify spatiotemporal changes in the accumulation

361 of payloads in brain tumors. GBM12 cells that stably express Red Fluorescent Protein (GBM12-RFP)

362 were implanted into NSG mice intracranially, and either Cy5.5 conjugate **8**, **9**, or **10** was administered

363 intravenously at 3 mg/kg 14 days post-implantation (**Figure 6A**). Fluorescence images were then taken

364 at multiple time points through a cranial window. As demonstrated by the increasing RFP signals, the

365 implanted tumors continued to grow throughout the study (**Figures 6B–D**). To offset the intragroup and

366 intergroup variances derived from tumor growth, the Cy5.5 signal intensity was normalized to the RFP

367 signal intensity at each time point. The intratumor concentrations of the three conjugates peaked

368 around Day 3 post-administration and then declined over time (**Figure 6E**). Notably, homogeneous

369 conjugate **8** accumulated in the orthotopic GBM12 tumors more significantly and persistently than

370 heterogeneous variants **9** and **10**; the statistically significant enhancement was observed for up to 5

371 days (**Figure 6E**). Overall, these results suggest that homogeneous conjugation allows intravenously

372 administered antibody conjugates to target brain tumors with enhanced payload delivery efficiency and

373 durability.

18
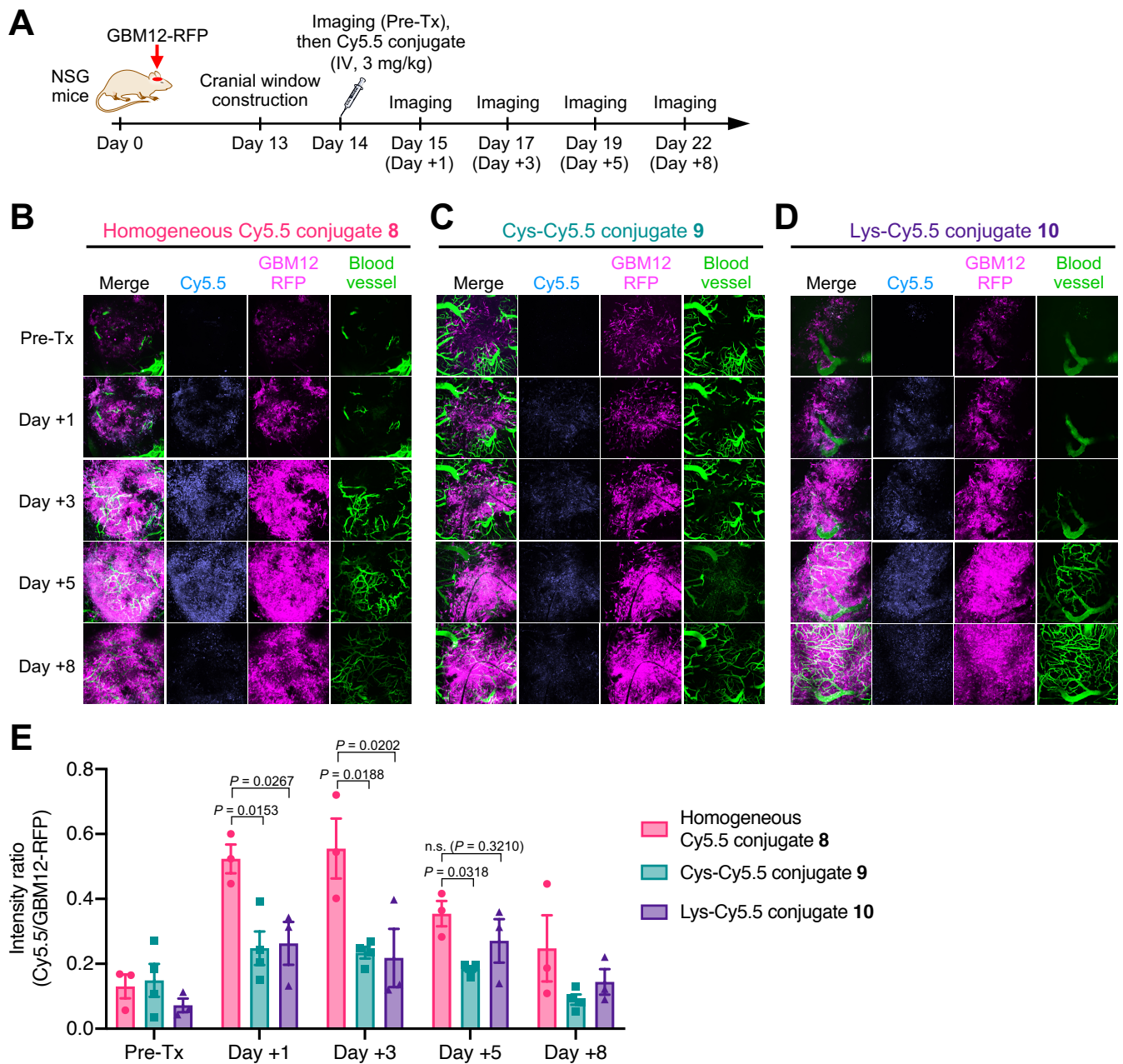
Figure 6. Homogeneous conjugation allows for enhanced payload delivery to orthotopically xenografted GBM tumors for several days. **A** Study schedule for intravital imaging. Male NSG mice were intracranially implanted with GBM12-RFP cells. Thirteen days after tumor implantation, a cranial window was constructed in each animal. Next day, each group was then injected intravenously with a single dose of each Cy5.5 conjugate at 3 mg/kg. Fluorescence images were taken before administration (Pre-Tx) and on Day 1, 3, 5, and 8 post-administration. FITC-conjugated dextran was injected right before each imaging session to visualize the brain microvasculature. **B** Intravital images of GBM12-RFP tumors treated with homogeneous Cy5.5 conjugate **8** (n = 3). A representative image at each time point is shown. **C** Intravital images of GBM12-RFP tumors treated with Cys-Cy5.5 conjugate

384   **9** (n = 4). A representative image at each time point is shown. **D** Intravital images of GBM12-RFP

385   tumors treated with Lys-Cy5.5 conjugate **10** (n = 3). A representative image at each time point is

386   shown. Cy5.5, cyan; RFP, magenta; FITC, green. **E** Normalized Cy5.5 intensity (Cy5.5 signal/GBM12-

387   RFP signal). Data are presented as mean values ± SEM. For statistical analysis, a one-way ANOVA

388   with a Dunnett's post hoc test (control: homogeneous conjugate **8**) was used (see **Table S4** for details).

389

390   **High-DAR components in heterogeneous MMAF ADCs target brain tumors less efficiently than**

391   **low-DAR components**

392   Finally, we set out to clarify underlying mechanisms attenuating the brain tumor targeting efficiency

393   of heterogeneous ADCs. To investigate how each DAR component could affect biodistribution profiles,

394   we prepared depatuxizumab-based MMAF ADCs with DARs of 4, 6, and 8 using our branched linkers

395   and non-cleavable BCN–MMAF (see Supplementary Information for synthesis details). The parent

396   N297A depatuxizumab was used as a DAR 0 control. These anti-EGFRvIII mAbs and conjugates were

397   then labeled with Cy5.5 NHS ester at DOL of 2.3–2.5 to afford DAR 0 mAb **11**, DAR 4 ADC **12**, DAR 6

398   ADC **13**, and DAR 8 ADC **14** (**Figures 7A** and **S8**). Cy5.5 was installed directly onto the mAb scaffold

399   so that the fluorescent signal would represent the localization of the entire ADC molecule. The

400   fluorescent conjugates (3 mg/kg) were injected intravenously into NSG mice bearing orthotopic

401   U87ΔEGFR-luc tumors on Day 5 post tumor implantation. After blood collection and cardiac perfusion

402   at 48 h, major organs were harvested for fluorescence imaging. DAR 0 and DAR 4 conjugates **11** and

403   **12** showed similar levels of brain tumor accumulation (**Figures 7B** and **7C**). In contrast, compared with

404   DAR 4 ADC **12**, markedly attenuated brain tumor accumulation was observed for DAR 6 ADC **13** ($P =$

405   0.0396) and DAR 8 ADC **14** ($P = 0.0288$). Although ADCs **12**–**14** accumulated in the liver more

406   significantly than DAR 0 mAb **11**, the degrees of liver accumulation and biodistribution patterns of these

407   ADCs were similar and irrespective of DAR (**Figures 7D** and **7E**). In addition, the concentrations of

408   DAR 4 and 6 ADCs **12** and **13** in blood were in a similar range and slightly below that of DAR 0 mAb **11**

409   (**Figure 7F**). DAR 8 ADC **14** underwent accelerated clearance from the circulation probably because of

410   greatly increased hydrophobicity. Collectively, these results demonstrate that high DAR components

411 comprising a given heterogeneous ADC can show poor brain tumor targeting compared to components

412 with optimal or low DARs, leading to reduced payload delivery efficiency.

413
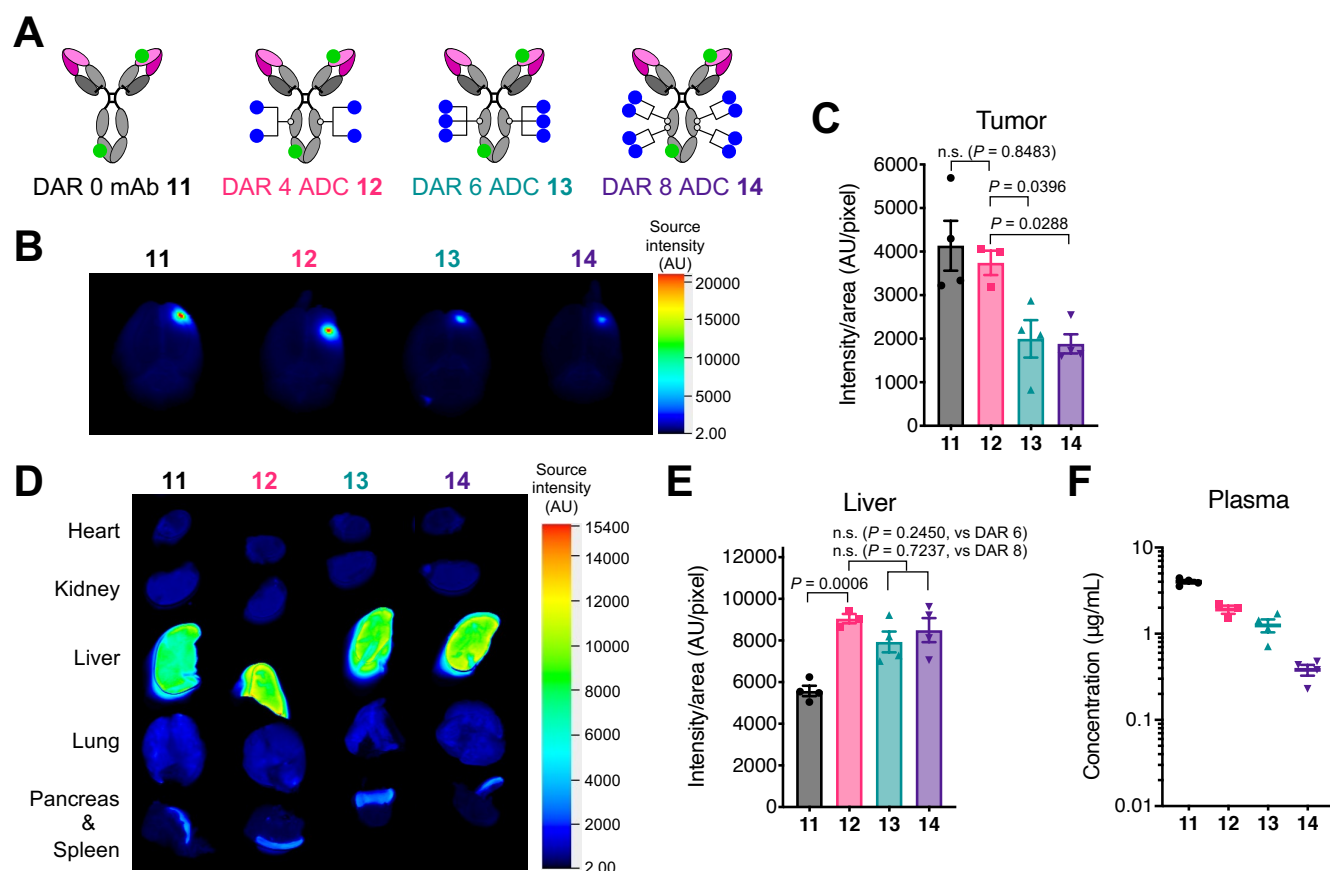
414

415 **Figure 7.** High-DAR components in heterogeneous ADCs target brain tumors less efficiently than

416 components with optimal or low DAR. **A** Structures of fluorescently labeled anti-EGFRvIII ADCs

417 equipped MMAF (blue circle) at DARs of 0, 4, 6, and 8. Cy5.5 (green circle) was conjugated by lysine

418 coupling at DOL of 2.3–2.5. **B** Ex vivo fluorescence images of whole brains harvested from NSG mice

419 bearing orthotopic U87ΔEGFR-luc tumors 48 hours after intravenous injection of each fluorescent ADC

420 (n = 3 for DAR 4 ADC **12**; n = 4 for all other groups). Images were taken using a 700 nm channel. **C**

421 Semi-quantification of the Cy5.5 signal derived from the tumor lesions in the whole brains. DAR 0 mAb

422 **11** (black), DAR 4 ADC **12** (magenta), DAR 6 ADC **13** (green), and DAR 8 ADC **14** (purple). **D** Ex vivo

423 fluorescence images of other major organs. **E** Semi-quantification of the Cy5.5 signal detected in the

424 liver. **F** Concentrations in plasma. Blood was collected 48 h post ADC injection (right before cardiac

425 perfusion) to quantify total antibody by sandwich ELISA. A representative image from each group is

426 shown in all panels of fluorescence images. Data are presented as mean values ± SEM. For statistical

21

427   analysis, a one-way ANOVA with a Dunnett's post hoc test (control: DAR 4 ADC **12**) was used (see

428   **Table S4** for details).

429

430   **DISCUSSION**

431   We have investigated how ADC homogeneity impacts therapeutic efficacy and survival extension in

432   orthotopic brain tumor models. Our stepwise conjugation method (i.e., MTGase-mediated site-specific

433   linker conjugation and following click reaction) efficiently generated homogeneous ADCs targeting

434   EGFR, EGFRvIII, and HER2. We tested these homogeneous ADCs and their heterogeneous variants

435   prepared by conventional lysine or cysteine coupling for antiproliferative effect against brain tumor cells.

436   In vitro, all DAR-matched ADCs showed comparable antigen-specific binding and cell killing potency

437   irrespective of ADC homogeneity, conjugation method, or linker cleavability. However, we obtained

438   contrasting results *in vivo*; all homogeneous ADCs exerted far better survival benefits in both cell line-

439   derived xenograft and PDX orthotopic brain tumor models than could be achieved by corresponding

440   heterogeneous variants, including a Depatux-M surrogate. Notably, a single dose of our homogeneous

441   ADCs at 3 mg/kg provided complete remission in the orthotopic U87ΔEGFR-luc (2 out of 6 mice by anti-

442   EGFR ADC **1**; 4 out of 6 mice by anti-EGFRvIII ADC **4**) and JIMT1-BR3 models (6 out of 6 mice by

443   anti-HER2 ADC **6**), whereas DAR-matched heterogeneous ADCs did not in either case. To delve into

444   this discrepancy, we performed biodistribution studies using intracranially xenografted GBM models.

445   Our data from these studies indicate that homogeneous conjugation at optimal DARs likely allows for

446   enhanced and persistent payload accumulation into intracranial tumors over several days, leading to

447   improved *in vivo* efficacy. We also confirmed that both cleavable and non-cleavable linkers allowed

448   homogeneous anti-EGFR conjugates to deliver payloads to intracranial GBM tumors at similar levels.

449   Collectively, these results demonstrate that ADC homogeneity is a critical factor determining

450   therapeutic efficacy in the treatment of brain tumors.

451

452   The question we asked next is how ADC homogeneity critically influences systemic payload

453   delivery to brain tumors. Many studies have shown that homogeneous ADCs provide more favorable

22

454   therapeutic effects in the treatment of other solid tumors than can be achieved by heterogeneous

455   variants (Bryant et al., 2015; Junutula et al., 2008, 2010; Lhospice et al., 2015; Pillow et al., 2014).

456   Nevertheless, the improvement in therapeutic efficacy observed in our study appears to be much more

457   prominent compared to those cases. We think that blockage of drug influx by an intact BBB in and

458   around brain tumors likely answers this question. The BBB was believed to be uniformly and

459   significantly disrupted in most GBM tumors. Contrary to this previous belief, recent preclinical and

460   clinical studies have demonstrated that a measurable number of GBM cells, in particular ones near the

461   growing edge of the infiltrative tumor area, exist behind an intact BBB or partially functional blood–

462   tumor barrier (BTB) (Arvanitis et al., 2020; Kim et al., 2018; Marin et al., 2021; Sarkaria et al., 2018; van

463   Tellingen et al., 2015). As such, GBM cells protected by an intact BBB are inaccessible to systemically

464   administered ADCs. Recently, Sarkaria and co-workers exhaustively validated heterogeneous BBB

465   disruption in multiple PDX models of GBM, including GBM12 (Marin et al., 2021). They also

466   demonstrated that the intact BBB likely caused an uneven intracranial distribution of systemically

467   administered Depatux-M, resulting in insignificant treatment outcomes in 5 out of 7 orthotopic PDX

468   models. In contrast, they found that Depatux-M exerted remarkable therapeutic effects when tested in

469   subcutaneous models of the same PDX tumors, in which the BBB did not constitute the tumor

470   microenvironment. This report highlights the importance of testing ADCs for brain tumor treatment in

471   clinically relevant orthotopic models rather than subcutaneous models.

472

473   Our findings and the report from the Sarkaria group (Marin et al., 2021) lead to a hypothesis that

474   high-DAR species included in heterogeneous ADCs cannot be efficiently delivered to intracranial

475   tumors across the BBB compared to low-DAR species. Consequently, the effective DAR (i.e., DARs

476   adjusted based on the brain tumor targeting efficiency of each DAR component relative to that of the

477   unmodified mAb) and payload dose are considerably reduced (**Figure 8**). In contrast, homogeneous

478   ADCs constructed at optimal DARs likely undergo only marginal impairment in brain tumor targeting,

479   leading to a minimal reduction in effective payload dose. Indeed, our intravital imaging study showed

480 that the difference in payload dose between heterogeneous and homogeneous ADCs could reach up to

481 2.5-fold. In general, ADC hydrophobicity increases in proportion to the degree of payload conjugation.

482 As such, high-DAR ADCs have greater aggregation tendency compared with low-DAR ADCs. In

483 circulation, such multimolecular complexation may also occur with abundant proteins such as albumin,

484 resulting in increased apparent hydrodynamic radius (Frka-Petesic et al., 2016). Considering that BBB

485 permeability declines exponentially with molecular size (Li et al., 2016), we speculate that an increase

486 in apparent hydrodynamic radius is disadvantageous for delivering conjugated payloads to brain tumors

487 across the intact BBB or partially functional BTB. As demonstrated in our treatment study using the

488 intracranial JIMT-1-BR3 tumor model (i.e., complete remission in all animals by homogeneous ADC **6**

489 vs no complete remission by heterogeneous ADC **7**), a decrease in the effective DAR by

490 heterogeneous conjugation could be further prominent in grade 1–3 gliomas and HER2-positive brain

491 metastatic tumors, in which BBB disruption is less significant than in GBM (Gril et al., 2020; Yonemori

492 et al., 2010). The use of more hydrophobic payloads than MMAF may also make this effect salient. As

493 observed in previous studies using other solid tumor models (Hamblett et al., 2004; Lhospice et al.,

494 2015), clearance and *in vivo* stability of ADCs could also be factors influencing payload delivery

495 efficiency and overall treatment efficacy in orthotopic brain tumor models. Indeed, we observed

496 promoted clearance for DAR 8 MMAF ADC **14**. However, DAR 6 ADC **13**, which also showed poor

497 brain tumor targeting, did not undergo rapid clearance. In addition, the treatment efficacy of

498 heterogeneous Cys conjugate **2** in the orthotopic U87ΔEGFR-luc tumor model was comparable to that

499 of Lys conjugate **3**, despite its impaired thermal and circulation stability. Overall, these findings support

500 the conclusion that ADC homogeneity can influence payload delivery to brain tumors across the BBB

501 more significantly than clearance and *in vivo* stability profiles. Future in-depth structural and

502 mechanistic studies will clarify the validity of our hypothesis in other combinations of mAbs, linker and

503 conjugation chemistries, and payload types.

504

24
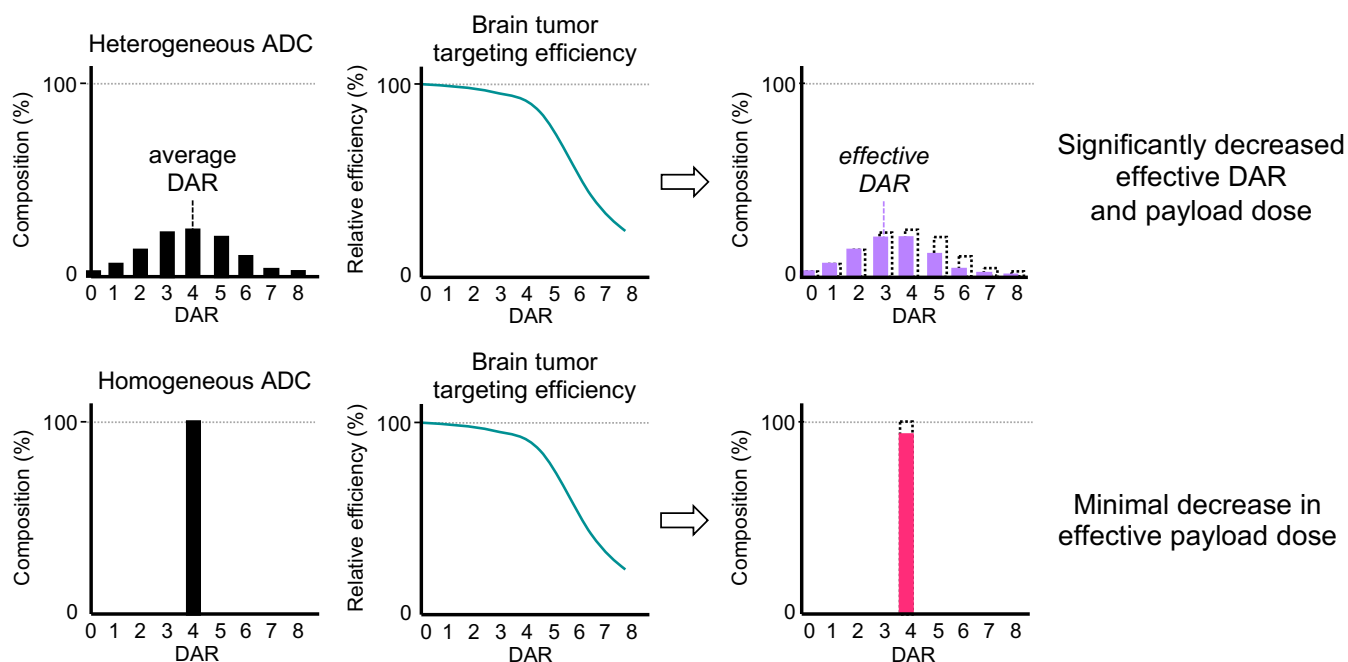
Figure 8. Reduction in effective DAR and payload dose is more prominent in heterogeneous ADCs than in homogeneous ADCs. All values used in this figure are estimated values based on the data shown in **Figures 1** and **7**. Theoretical payload doses of heterogeneous and homogeneous ADCs with the same (average) DAR are equivalent if administered at the same mAb dose. However, high-DAR components in heterogeneous ADCs show poor brain tumor targeting, decreasing the effective DAR and payload dose. Such deterioration is marginal in the case of homogeneous ADCs, leading to improved payload delivery and overall efficacy.

In summary, our findings highlight the critical importance of ADC homogeneity in maximizing efficacy in brain tumor treatment. Employing homogeneous conjugation at optimal DARs with properly designed linkers could be a promising approach to resurrecting the ADCs for GBM that have failed to show therapeutic benefits in clinical trials, including Depatux-M. We also envision that initiating exploration of new ADCs using homogeneous conjugation technologies will help streamline the optimization of ADC properties (e.g., DAR, hydrophobicity, stability) and effectively expand our repertoire of promising drug candidates for brain tumors. In addition to this updated molecular design guideline, further understanding of brain tumor biology and pathophysiology will also be crucial to identify promising combinations of antibody targets, ADC linker properties (e.g., structure, drug release mechanism), and payload types. In particular, deeper understanding of the integrity and functions of the

25

524 BBB found in patient-derived brain tumor samples could open up the next step to improving payload

525 delivery efficiency. We believe that such multifaceted approaches will finally lead us to novel ADCs or

526 other targeted therapy modalities with the potential to conquer GBM and other intractable brain tumors.

527

539

540 **AUTHOR CONTRIBUTIONS**

541 Conceptualization, K.T.; Methodology, Y.A., Y.O., W.X., N.Z., Z.A., B.K., and K.T.; Validation, Y.A.,

542 Y.O., and W.X.; Formal Analysis, Y.A., Y.O., S.Y.Y.H; Investigation, Y.A., Y.O., W.X., S.Y.Y.H, A.Y.,

543 and K.T.; Resources, N.Z., Z.A., B.K., and K.T.; Writing – Original Draft, Y.A., Y.O., and K.T.; Writing –

544 Review & Editing, Y.A., Y.O., A.Y., Z.A., and K.T.; Visualization, Y.A. and Y.O.; Supervision, K.T.;

545 Project Administration, K.T.; Funding Acquisition, Y.A., A.Y., Z.A., B.K., and K.T.

546

547

548

549

550 **DECLARATION OF INTERESTS**

551 Y.A., N.Z., Z.A., and K.T. are named inventors on a patent application relating to the work filed by the

552 Board of Regents of the University of Texas System (PCT/US2018/034363; US-2020-0115326-A1;

553 EU18804968.8-1109/3630189). The remaining authors declare no competing interests.

554

555 **METHODS**

556 **Compounds and antibody conjugates**

557 See Supplementary Information for synthesis details and characterization data of all compounds used

558 in this study.

559

560 **Antibodies**

561 Anti-EGFR, anti-EGFRvIII, and anti-HER2 IgG1 mAbs with N88A/N297A, N297A, or N297Q mutation

562 were expressed in-house (see below). The other antibodies used in this study were purchased from

563 commercial vendors as follows: Rabbit anti-MMAF antibody (LEV-PAF1) from Levena Biopharma; goat

564 anti-human IgG Fab-horseradish peroxidase (HRP) conjugate (109-035-097), goat anti-human IgG Fc

565 antibody (109-005-098), and donkey anti-human IgG-HRP conjugate (709-035-149) from Jackson

566 ImmunoResearch; goat anti-rabbit IgG–HRP conjugate (32260) from Thermo Fisher Scientific; rabbit

567 anti-cleaved caspase 3 antibody (9661S) and rabbit anti-EGFR antibody (4267S) from Cell Signaling

568 Technology); and rabbit anti-Ki67 antibody (ab16667) from Abcam.

569

570 **Expression and purification of human monoclonal antibodies**

571 All human monoclonal antibodies were produced according to the procedure reported previously(Anami

572 et al., 2017; Shi et al., 2014). Briefly, free style HEK-293 human embryonic kidney cells (Invitrogen)

573 were transfected with a mammalian expression vector encoding for the human IgG1 kappa light chain

574 and full-length heavy chain sequences (based on variable sequences of cetuximab, depatuxizumab, or

575 trastuzumab). The transfected HEK-293 cells were cultured in a humidified cell culture incubator at

27

576 37 °C with 8% CO_2 and shaking at 150 rpm for 7 days before harvesting the culture medium. The

577 antibody secreted into the culture medium was purified using Protein A resin (GE Healthcare).

578

579 **MTGase-mediated antibody–linker conjugation**

580 Anti-EGFR mAb with N88A/N297A double mutations (400 µL in PBS, 5.53 mg/mL, 2.21 mg antibody)

581 was incubated with the diazide branched linker developed by us previously (Anami et al., 2017, 2018)

582 (5.9 µL of 100 mM stock in water, 40 equiv.) and Activa TI® (101 µL of 40% solution in PBS, Ajinomoto,

583 purchased from Modernist Pantry) at room temperature for 22 h. The reaction was monitored using

584 either 1) an Agilent LC-MS system consisting of a 1100 HPLC and a 1946D single quadrupole ESI

585 mass spectrometer equipped with a MabPac RP column (3 × 50 mm, 4 µm, Thermo Scientific) or 2) a

586 Thermo LC-MS system consisting of a Vanquish UHPLC and a Q Exactive™ Hybrid Quadrupole-

587 Orbitrap™ Mass Spectrometer equipped with a MabPac RP column (2.1 × 50 mm, 4 µm, Thermo

588 Scientific). Elution conditions were as follows: mobile phase A = water (0.1% formic acid); mobile phase

589 B = acetonitrile (0.1% formic acid); gradient over 6.8 min from A:B = 75:25 to 1:99; flow rate = 0.5

590 mL/min. The conjugated antibody was purified by SEC (Superdex 200 increase 10/300 GL, GE

591 Healthcare, solvent: PBS, flow rate = 0.6 mL/min) to afford an antibody–linker conjugate [1.91 mg, 86%

592 yield determined by bicinchoninic acid (BCA) assay].

593

594 **Construction of homogeneous ADCs by strain-promoted azide−alkyne cycloaddition**

595 BCN–EVCit–PABC–MMAF (20.7 µL of 3.7 mM stock solution in DMSO, 1.5 equivalent per azide group)

596 was added to a solution of the mAb–linker conjugate in PBS (460 µL, 4.16 mg/mL), and the mixture

597 was incubated at room temperature for 22 h. The reaction was monitored using either Agilent LC-MS

598 system or Thermo LC-MS system equipped with a MabPac RP column (see above) and the crude

599 products were purified by SEC to afford homogeneous ADC **1** (1.71 mg, 90% yield determined by BCA

600 assay). Analysis and purification conditions were the same as described above. Homogeneity was

28

601 confirmed by ESI-MS analysis. Homogeneous anti-EGFRvIII ADC **4** and anti-HER2 ADC **6** were

602 prepared in the same manner.

603

604 **Construction of a heterogeneous ADC by cysteine conjugation**

605 Aglycosylated anti-EGFR mAb (298 μL in PBS, 3.0 mg/mL, 895 μg antibody) was mixed with TCEP

606 (19.1 μL of 1 mM stock solution in water, 3.2 equiv.) and EDTA (30 μL of 10 mM stock solution in water,

607 pH 9, 10% v/v) and incubated at 37 ºC for 2 h. MC–MMAF (9.0 μL of 10 mM stock solution in DMSO,

608 15 equiv.) was added to the partially reduced mAb solution and the reaction mixture was incubated

609 overnight at room temperature. The reaction was monitored using an Agilent 1100 HPLC system

610 equipped with a MAbPac HIC-Butyl column (4.6 × 100 mm, 5 μm, Thermo Scientific). Elution conditions

611 were as follows: mobile phase A = 50 mM sodium phosphate containing ammonium sulfate (1.5 M) and

612 5% isopropanol (pH 7.4); mobile phase B = 50 mM sodium phosphate containing 20% isopropanol (pH

613 7.4); gradient over 25 min from A:B = 99:1 to 1:99; flow rate = 0.8 mL/min. *N*-acetyl cysteine (4.5 μL of

614 100 mM stock solution in DMSO, 75 equiv.) was added to the reaction mixture for quenching the

615 reaction. The crude products were purified by SEC to afford Cys conjugate **2** (668 μg, 75% yield

616 determined by BCA assay, average DAR: 3.8). SEC purification conditions were the same as described

617 above. The average DAR value was determined based on UV peak areas in HIC analysis.

618

619 **Construction of heterogeneous ADCs by lysine conjugation**

620 Aglycosylated anti-EGFR mAb (105 μL in PBS, 3.0 mg/mL, 315 μg antibody) was mixed with 1 M

621 phosphate solution at pH 9 (10.5 μL) and MMAF-NHS (2.5 μL of 10 mM stock solution in DMSO, 12

622 equiv.) and the mixture was incubated at room temperature for 3 h. The reaction was monitored using

623 either Agilent LC-MS system or Thermo LC-MS system equipped with a MabPac RP column (see

624 above). The crude products were purified by SEC to afford Lys conjugate **3** (197 μg, 63% yield

625 determined by BCA assay, average DAR: 3.9). Analysis and purification conditions were the same as

626 described above. The average DAR value was determined based on ion intensity of each DAR species

29

627   in ESI-MS analysis. Heterogeneous anti-EGFRvIII ADC **5** and anti-HER2 ADC **7** were constructed in

628   the same manner.

629

630   **Construction of anti-EGFR Cy5.5 conjugates**

631   Cy5.5 conjugates **8–10** were prepared in the same manner as the preparation of corresponding ADCs

632   described above. Instead of MMAF-containing linker modules, either of the following linker modules

633   were used: DBCO–EVCit–Cy5.5 (synthesized in house, for homogeneous Cy5.5 conjugate **8**), Cy5.5

634   maleimide (purchased from Click Chemistry Tools, for Cys-Cy5.5 conjugate **9**), Cy5.5-NHS ester

635   (purchased from Click Chemistry Tools, for Lys-cy5.5 conjugate **10**), or DBCO–Cy5.5 (purchased from

636   Click Chemistry Tools, for homogeneous non-cleavable Cy5.5 conjugate). Degrees of labeling (DOL)

637   were determined by ESI-MS analysis (based on ion intensity of each DOL species) or using a plate

638   reader (BioTek Synergy HTX) with a standard curve for free Cy5.5 (absorbance at 680 nm).

639

640   **Construction of anti-EGFRvIII MMAF-Cy5,5 conjugates**

641   Homogeneous anti-EGFRvIII MMAF ADCs with DARs of 4, 6, and 8 were prepared from

642   depatuxizumab with an N297A (for DAR 4 and 6) or N297Q mutation (for DAR 8). For the preparation

643   of the DAR 6 MMAF ADC, the diazido-methyltetrazine tri-arm linker developed by us previously

644   (Yamazaki et al., 2021) was used. Subsequently, unmodified N297A depatuxizumab (DAR 0) and each

645   ADC were labeled with Cy5.5-NHS ester (10 mM stock solution in DMSO, 6–8 equiv.) to achieve an

646   average DOL of 2.3–2.5. The labeling reaction was performed in the same manner as described above,

647   except that the reaction was quenched with ethanol amine (100 mM stock solution in water, 20 equiv.).

648   The average DOL values of MMAF-Cy5.5 conjugates **11**–**14** were determined based on ion intensity of

649   each DOL species in ESI-MS analysis.

650

651

652

30

653 **Long-term stability test**

654 Each ADC (1 mg/mL, 10 μL) in PBS was incubated at 37 °C for 28 days and stored at −80 °C until use.

655 Samples were analyzed using an Agilent 1100 HPLC system equipped with a MAbPac SEC-1

656 analytical column (4.0 × 300 mm, 5 μm, Thermo Scientific). The conditions were as follows: flow rate =

657 0.2 mL/min; solvent = PBS. All assays were performed in triplicate.

658

659 **Cell lines**

660 U87ΔEGFR was received from Dr. Erwin G. Van Meir (Emory University). Gli36δEGFR was received

661 from Dr. E. Antonio Chiocca (Brigham and Women's Hospital, Harvard Medical School). U87ΔEGFR-

662 luc was generated by lentiviral transduction of U87ΔEGFR cells using Lentifect™ lentiviral particles

663 encoding for firefly luciferase and a puromycin-resistant gene (GeneCopoeia, LP461-025).

664 Transduction was performed according to the manufacturer's instruction. U87ΔEGFR, U87ΔEGFR-luc,

665 Gli36δEGFR, and HEK293 (ATCC) cells were cultured in DMEM (Corning) supplemented with 10%

666 EquaFETAL® (Atlas Biologicals), GlutaMAX® (2 mM, Gibco), and penicillin-streptomycin (penicillin: 100

667 units/mL; streptomycin: 100 μg/mL, Gibco). JIMT1-BR3 was received from Dr. Patricia S. Steeg

668 (National Cancer Institute) and maintained in RPMI1640 (Corning) supplemented with 10%

669 EquaFETAL®, GlutaMAX® (2 mM), sodium pyruvate (1 mM, Corning), and penicillin-streptomycin

670 (penicillin: 100 units/mL; streptomycin: 100 μg/mL). GBM12 was received from Dr. Jann N. Sarkaria

671 (Mayo Clinic). RFP-expressing GBM12 (GBM12-RFP) was generated by transduction with lentivirus

672 (System Biosciences, LL110VA-1) according to the manufacturer's instruction. GBM12 and GBM12-

673 RFP cells were maintained in DMEM supplemented with 2% fetal bovine serum and penicillin-

674 streptomycin (penicillin: 100 units/mL; streptomycin: 100 μg/mL). All cells except U87ΔEGFR-luc and

675 HEK293 were authenticated via short tandem repeat profiling before use. All cells were cultured at

676 37 °C under 5% CO_2, and passaged before becoming fully confluent up to 40 passages. All cells were

677 periodically tested for mycoplasma contamination.

678

Cell-based ELISA

Cells (U87ΔEGFR or HEK293) were seeded in a culture-treated 96-well clear plate (10,000 cells/well in 100 µL culture medium) and incubated at 37 °C with 5% CO_2 for 24 h. Paraformaldehyde (8%, 100 µL) was added to each well and incubated for 15 min at room temperature. The medium was discarded and the cells were washed three times with 100 µL of PBS. Cells were treated with 100 µL of blocking buffer (0.2% BSA in PBS) with agitation at room temperature for 2 h. After the blocking buffer was discarded, serially diluted samples (in 100 µL PBS containing 0.1% BSA) were added and the plate was incubated overnight at 4 °C with agitation. The buffer was discarded and the cells were washed three times with 100 µL of PBS containing 0.25% Tween 20. Cells were then incubated with 100 µL of donkey anti-human IgG–HRP conjugate (diluted 1:10,000 in PBS containing 0.1% BSA) was added and the plate was incubated at room temperature for 1 h. The plate was washed three times with PBS containing 0.25% Tween 20, and 100 µL of 3,3´,5,5´-tetramethylbenzidine (TMB) substrate (0.1 mg/mL) in phosphate–citrate buffer/30% H_2O_2 (1:0.0003 volume to volume, pH 5) was added. After color was developed for 10−30 min, 25 µL of 3 N-HCl was added to each well and then the absorbance at 450 nm was recorded using a plate reader (BioTek Synergy HTX). Concentrations were calculated based on a standard curve. K_D values were then calculated using Graph Pad Prism 8 software. All assays were performed in triplicate.

Cell viability assay

Cells were seeded in a culture-treated 96-well clear plate (5,000 cells/well in 50 µL culture medium) and incubated at 37 °C under 5% CO_2 for 24 h. Serially diluted samples (50 µL) were added to each well and the plate was incubated at 37 °C for 72 h. After the old medium was replaced with 100 µL fresh medium, 20 µL of a mixture of WST-8 (1.5 mg/mL, Cayman chemical) and 1-methoxy-5-methylphenazinium methylsulfate (100 µM, Cayman Chemical) was added to each well, and the plate was incubated at 37 °C for 2 h. After gently agitating the plate, the absorbance at 460 nm was recorded

704   using a plate reader (BioTek Synergy HTX). EC_{50} values were calculated using Graph Pad Prism 8

705   software. All assays were performed in triplicate.

706

707   Animal studies

708   All procedures were approved by the Animal Welfare Committee of the University of Texas Health

709   Science Center at Houston and performed in accordance with the institutional guidelines for animal

710   care and use. All animals were housed under controlled conditions, namely 21–22 °C (+/- 0.5 °C), 30–

711   75% (+/-10%) relative humidity, and 12:12 light/dark cycle with lights on at 7.00 a.m. Food and water

712   were available ad libitum for all animals. NSG mice were purchased from The Jackson Laboratory

713   (stock number: 005557) and bred in house. CD-1® mice was purchased from Charles River

714   Laboratories (Strain Code: 022) and used without in-house breeding.

715

716   Orthotopic xenograft mouse models of human brain tumors

717   U87ΔEGFR-luc (1×10^5 cells), GBM12 (2×10^5 cells), or JIMT1-BR3 (2×10^5 cells) were

718   stereotactically implanted into NSG mice (6–8 weeks old, male and female) based on the previously

719   reported method (Otani et al., 2020). Typical procedure. NSG mice were injected intraperitoneally with

720   a cocktail of ketamine (67.5 mg/kg) and dexmedetomidine (0.45 mg/kg) and maintained at 37 °C on a

721   heating pad until the completion of surgery. After the head skin was shaved and treated with 10 μL of

722   0.25% bupivacaine supplemented with epinephrine (1:200,000), anesthetized mice were placed on a

723   stereotactic instrument. After disinfecting the head skin with chlorhexidine and ethanol, a small incision

724   was made and then a burr hose was drilled into the skull over the right hemisphere (1 mm anterior and

725   2 mm lateral to the bregma). A 10 μL Hamilton syringe (model 701 N) was loaded with cells suspended

726   in 2 μL cold hanks-balanced salt solution (HBSS) and slowly inserted into the right hemisphere through

727   the burr hole (3.5 mm depth). After a 1-min hold time, cells were injected over a 5-min period (0.4

728   μL/min). After a 3-min hold time, the needle was retracted at a rate of 0.75 mm/min. The incision was

729   closed using GLUture® (Zoetis) and mice were injected with atipamezole (1 mg/kg, i.p.).

33

730 **Treatment study**

731 Brain tumor-bearing NSG mice were randomized and injected intravenously with a single dose of either

732 ADC (3 mg/kg) or PBS. Group assignment and dose schedule were as follows: U87ΔEGFR-luc model,

733 n = 4 or 6 for vehicle, n = 6 for ADCs, injected on Day 5; GBM12 model, n = 15 for vehicle, n = 14 for

734 ADCs injected on Day 8; JIMT-1-BR3 model, n = 6 for all groups, injected on Day 7. Growth of

735 U87ΔEGFR-luc tumors was monitored by bioluminescence imaging (BLI) using an Xtreme *in vivo*

736 imager (Bruker Biospin, upper limit: 1.5×10^5 photons/sec/mm^2; lower limit: 5.0×10^3 photons/sec/mm^2)

737 once every week. Tumor growth was also evaluated by MRI (see the following sections for details).

738 Body weight was monitored every 3–4 days and mice were euthanized when body weight loss of >20%

739 or any severe clinical symptom was observed.

740

741 **MRI and measurement of tumor volume (GBM12 model)**

742 MRI was performed using a 7 Tesla MRI scanner (Bruker Biospin) on Day 18 post tumor implantation.

743 Tumor-bearing mice (n = 4/group, randomly selected from each group) were anesthetized with 1.5%

744 isoflurane in a 30:70 mixture of O_2 and medical air. MRI contrast agent (Dotarem) was injected (50 μL,

745 i.p.) before imaging to help visualize the tumor. T2-weighted images were acquired using a multi-echo

746 RARE sequence with a RARE factor of 3. Acquisition parameters were as follows: TR = 5000 ms, TE =

747 17 42.5 68 and 93.5 ms, 15 image slices with 100 μm slice thickness, in-plane resolution = 100 × 100

748 μm^2. ImageJ software was utilized to measure the tumor volume. Regions of interest (ROI) were

749 manually drawn to circumscribe the entire tumor, and volume was calculated by counting all the voxels

750 within the ROI and multiplying the total number of pixels by the volume of the voxel (100 × 100 × 500

751 μm^3).

752

753 **MRI in the U87ΔEGFR-luc and JIMT-1-BR3 models**

754 MRI images were taken using a 7 Tesla MRI scanner (Bruker Biospin) on Day 58 (JIMT-1-BR3) or Day

755 61 (U87ΔEGFR-luc) post tumor implantation. Tumor-bearing mice (U87ΔEGFR-luc model: 4 survivor

34

756 mice treated with homogeneous anti-EGFRvIII ADC **4**; JIMT-1: n = 6/group) were anesthetized with 2%

757 isoflurane throughout the imaging procedure. A 35mm ID volume coil (Bruker Biospin) receive setup

758 was used for data acquisition. T2-weighted coronal and axial images were acquired with a Spin Echo

759 RARE sequence. Acquisition parameters were as follows: TR = 3000 ms, TE =57 ms, RARE factor 12,

760 6 NAV, Slice thickness of 0.75 mm, slice gap 0.25 mm, in plane resolution of 156 μm for coronal and

761 117 μm for axial.

762

763 **Immunohistochemistry**

764 Mice were euthanized at the end of the treatment study in the GBM12 model and their excised tumor-

765 bearing brain were embedded in paraffin. Samples were deparaffinized using xylene and rehydrated in

766 decreasing concentration of ethanol. Subsequently, slices were incubated in 0.3% H_2O_2 for 30 min and

767 autoclaved for 15 min at 121ºC in citrate buffer. After blocking with animal-free blocking solution, slices

768 were incubated with either rabbit anti-cCaspase 3 antibody (1:250), rabbit anti-EGFR antibody (1:50),

769 or rabbit anti-ki67 antibody (1:200). SignalStain® Boost IHC Detection Reagent and DAB substrate kit

770 (Cell Signaling Technology) were used and then the sections were counterstained with hematoxylin.

771 Bright-field images were taken using an EVOS-FL Auto2 imaging system (Invitrogen). For cleaved

772 caspase-3 and ki67 quantification, three representative areas of each stained sample were imaged and

773 the populations of cCaspase3- and ki67-positive cells were analyzed using Image J software.

774

775 **In vivo pharmacokinetic study**

776 CD-1® mice (6−8 weeks old, female, n = 3/group) were injected intravenously with each mAb or ADC (3

777 mg/kg). Blood samples (5 μL) were collected from each mouse via the tail vein at each time point (15

778 min, 6 h, 1 day, 2 days, 4 days, 9 days, and 14 days) and immediately processed with 495 μL of 5 mM

779 EDTA/PBS. After removal of cells by centrifugation (10 min at 10,000 × g at 4 °C), plasma samples

780 were stored at −80 °C until use. All mice were humanely killed after last blood collection. Plasma

781 samples were analyzed by sandwich ELISA. For determination of the total antibody concentration (both

782 conjugated and unconjugated), a high-binding 96-well plate (Corning) was treated with goat anti-human

783 IgG Fc antibody (500 ng/well). After overnight surface coating at 4 °C, the plate was blocked with 100

784 µL of 2% BSA in PBS containing 0.05% Tween 20 (PBS-T) with agitation at room temperature for 1 h.

785 Subsequently, the solution was removed and each diluted plasma sample (100 µL, diluted with PBS-T

786 containing 1% BSA) was added to each well, and the plate was incubated at room temperature for 2 h.

787 After each well was washed three times with 100 µL of PBS-T, 100 µL of goat anti-human IgG Fab–

788 HRP conjugate (1:5,000) was added. After being incubated at room temperature for 1 h, the plate was

789 washed and color development was performed as described above (see the section of "Cell-based

790 ELISA") . For determination of ADC concentration (conjugated only), assays were performed in the

791 same manner using the following proteins and antibodies: human EGFR (100 ng/well, #EGR-H5222

792 from ACROBiosystems) for plate coating, and rabbit anti-MMAF antibody (1:5,000) and goat anti-rabbit

793 IgG–HRP conjugate (1:10,000) as secondary and tertiary detection antibodies, respectively.

794 Concentrations were calculated based on a standard curve. Half-life at the elimination phase ($t_{1/2\beta}$, day)

795 and clearance rate [CL, (mg/kg)/(µg/mL)/day] of each conjugate were estimated using methods for non-

796 compartmental analysis (Gabrielsson and Weiner, 2012). PKSolver (a freely available menu-driven

797 add-in program for Microsoft Excel) (Zhang et al., 2010) was used for this calculation. Area under the

798 curve ($AUC_{0\text{-}14\text{ days}}$, µg/mL × day) was calculated using GraphPad Prism 8 software. See **Table S3** for

799 all observed PK parameters.

800

801 **Ex vivo fluorescence imaging and quantification**

802 Intracranial U87ΔEGFR-luc tumor-bearing NSG mice (6−8 weeks old, male and female) were prepared

803 as described above and randomized into three groups (n = 3) 5 days post tumor implantation. Each

804 Cy5.5 conjugate was administered intravenously at 3 mg/kg. After 48 h, the tumor-bearing mice were

805 anesthetized with ketamine/xylazine. Subsequently, the mice underwent cardiac perfusion with PBS(+)

806 containing sodium heparin (10 units/mL) and 4% paraformaldehyde/PBS(+). Major organs including the

807 brain were then harvested. Cy5.5-based near-infrared fluorescence images of the harvested organs

36

808   were taken using a LI-COR Odyssey 9120 imager (Ex: 685 nm laser, intensity: L1.0 for brain, L2.0 for

809   other organs, Em: 700 nm channel). Semi-quantification of the signals from ROIs was also performed

810   using LI-COR Image Studio software. For tissue imaging, the brain samples were embedded in paraffin

811   and tissue sections were prepared (thickness: 5 μm). After de-paraffinization of using toluene, mounting

812   medium containing DAPI (VECTOR #H-1200) was applied to the tissue slides. Fluorescence Images

813   were taken using a Nikon Eclipse TE2000E inverted microscope (Cy5 channel). Three ROIs in each

814   sample were acquired and analyzed for semi-quantification using ImageJ software.

815

816   **Intravital imaging**

817   Male NSG mice (6−8 weeks old) were implanted with GBM12-RFP cells (2×10^5 cells) stereotactically

818   into the right hemisphere (2 mm lateral and 2.5 mm posterior to bregma, 1 mm depth) as previously

819   described (Nair et al., 2020). Thirteen days after tumor implantation, craniectomy was performed over

820   the tumor-implanted area. Cover glass (Bioscience Tools) was placed on the brain surface and glued to

821   the skull with dental resin. Next day (Day 14), each Cy5.5 conjugate was administrated intravenously at

822   3 mg/kg (n = 4 for Cys-Cy5.5 conjugate **9**; n = 3 for the other groups). For intravital imaging, mice were

823   anesthetized with isoflurane and positioned on the stage of a A1R-MP confocal microscope (NIKON)

824   equipped with ×16 water immersion objective lens. Subsequently, 100 μL of 2% FITC-conjugated

825   dextran (500 kDa, Sigma) was administrated through the tail vein, and Z-stack images were acquired

826   based on Cy5.5, FITC, and RFP signals. Pre- and post-treatment images were acquired on Day 14, 15,

827   17, 19, and 22 after tumor implantation. The images were analyzed using NIS Elements AR software

828   (NIKON). Intensity of the RFP (derived from GBM12-RFP) and Cy5.5 signals in two or three

829   independent ROIs were calculated to determine Cy5.5/GBM12-RFP ratios.

830

831   **Statistical Analyses**

832   Kaplan-Meier survival curve statistics were analyzed with a log-rank (Mantel–Cox) test. To control the

833   family-wise error rate in multiple comparisons, crude *P* values were adjusted by the Bonferroni method.

834   Differences with adjusted *P* values <0.05 were considered statistically significant in all analysis. For

835   immunohistochemistry, immunofluorescence, ex vivo fluorescence imaging, MRI, and intravital imaging,

836   a one-way ANOVA with a Tukey–Kramer or Dunnett's post hoc test was used for multiple comparisons.

837   See **Table S4** for all *P* values.

838

839 **REFERENCES**

840 Abbott, N.J., Patabendige, A.A.K., Dolman, D.E.M., Yusof, S.R., and Begley, D.J. (2010). Structure and
841 function of the blood-brain barrier. Neurobiol. Dis. *37*, 13–25.

842 Anami, Y., and Tsuchikama, K. (2020). Transglutaminase-Mediated Conjugations. Methods Mol. Biol.
843 *2078*, 71–82.

844 Anami, Y., Xiong, W., Gui, X., Deng, M., Zhang, C.C., Zhang, N., An, Z., and Tsuchikama, K. (2017).
845 Enzymatic conjugation using branched linkers for constructing homogeneous antibody-drug conjugates
846 with high potency. Org. Biomol. Chem. *15*, 5635–5642.

847 Anami, Y., Yamazaki, C.M., Xiong, W., Gui, X., Zhang, N., An, Z., and Tsuchikama, K. (2018). Glutamic
848 acid-valine-citrulline linkers ensure stability and efficacy of antibody-drug conjugates in mice. Nat.
849 Commun. *9*, 2512.

850 Arvanitis, C.D., Ferraro, G.B., and Jain, R.K. (2020). The blood-brain barrier and blood-tumour barrier
851 in brain tumours and metastases. Nat. Rev. Cancer *20*, 26–41.

852 Banks, W.A. (2016). From blood-brain barrier to blood-brain interface: new opportunities for CNS drug
853 delivery. Nat. Rev. Drug Discov. *15*, 275–292.

854 Brennan, C.W., Verhaak, R.G.W., McKenna, A., Campos, B., Noushmehr, H., Salama, S.R., Zheng, S.,
855 Chakravarty, D., Sanborn, J.Z., Berman, S.H., et al. (2013). The somatic genomic landscape of
856 glioblastoma. Cell *155*, 462–477.

857 Bryant, P., Pabst, M., Badescu, G., Bird, M., McDowell, W., Jamieson, E., Swierkosz, J., Jurlewicz, K.,
858 Tommasi, R., Henseleit, K., et al. (2015). In Vitro and In Vivo Evaluation of Cysteine Rebridged
859 Trastuzumab-MMAE Antibody Drug Conjugates with Defined Drug-to-Antibody Ratios. Mol. Pharm. *12*,
860 1872–1879.

861 Chau, C.H., Steeg, P.S., and Figg, W.D. (2019). Antibody-drug conjugates for cancer. Lancet *394*,
862 793–804.

863 Chinot, O.L., Wick, W., Mason, W., Henriksson, R., Saran, F., Nishikawa, R., Carpentier, A.F., Hoang-
864 Xuan, K., Kavan, P., Cernea, D., et al. (2014). Bevacizumab plus radiotherapy-temozolomide for newly
865 diagnosed glioblastoma. N. Engl. J. Med. *370*, 709–722.

866 Deonarain, M., Yahioglu, G., and Bhatti, M. (2014). Biological materials and uses thereof.

867 Dhillon, S. (2018). Moxetumomab Pasudotox: First Global Approval. Drugs *78*, 1763–1767.

868 Doronina, S.O., Mendelsohn, B.A., Bovee, T.D., Cerveny, C.G., Alley, S.C., Meyer, D.L., Oflazoglu, E.,
869 Toki, B.E., Sanderson, R.J., Zabinski, R.F., et al. (2006). Enhanced activity of monomethylauristatin F
870 through monoclonal antibody delivery: effects of linker technology on efficacy and toxicity. Bioconjug.
871 Chem. *17*, 114–124.

872 Drago, J.Z., Modi, S., and Chandarlapaty, S. (2021). Unlocking the potential of antibody-drug
873 conjugates for cancer therapy. Nat. Rev. Clin. Oncol. *18*, 327–344.

874 Eli Lilly (2004). Erbitux (cetuximab) Label.

875 Frka-Petesic, B., Zanchi, D., Martin, N., Carayon, S., Huille, S., and Tribet, C. (2016). Aggregation of
876 Antibody Drug Conjugates at Room Temperature: SAXS and Light Scattering Evidence for Colloidal
877 Instability of a Specific Subpopulation. Langmuir *32*, 4848–4861.

878 Gabrielsson, J., and Weiner, D. (2012). Non-compartmental analysis. Methods Mol. Biol. *929*, 377–389.

879 Giddens, J.P., Lomino, J.V., DiLillo, D.J., Ravetch, J.V., and Wang, L.-X. (2018). Site-selective
880 chemoenzymatic glycoengineering of Fab and Fc glycans of a therapeutic antibody. Proc. Natl. Acad.
881 Sci. U. S. A. *115*, 12023–12027.

882 Gril, B., Wei, D., Zimmer, A.S., Robinson, C., Khan, I., Difilippantonio, S., Overstreet, M.G., and Steeg,
883 P.S. (2020). HER2 antibody-drug conjugate controls growth of breast cancer brain metastases in
884 hematogenous xenograft models, with heterogeneous blood-tumor barrier penetration unlinked to a
885 passive marker. Neuro. Oncol. *22*, 1625–1636.

886 Hamblett, K.J., Senter, P.D., Chace, D.F., Sun, M.M.C., Lenox, J., Cerveny, C.G., Kissler, K.M.,
887 Bernhardt, S.X., Kopcha, A.K., Zabinski, R.F., et al. (2004). Effects of drug loading on the antitumor
888 activity of a monoclonal antibody drug conjugate. Clin. Cancer Res. *10*, 7063–7070.

889 Hamblett, K.J., Kozlosky, C.J., Siu, S., Chang, W.S., Liu, H., Foltz, I.N., Trueblood, E.S., Meininger, D.,
890 Arora, T., Twomey, B., et al. (2015). AMG 595, an Anti-EGFRvIII Antibody-Drug Conjugate, Induces
891 Potent Antitumor Activity against EGFRvIII-Expressing Glioblastoma. Mol. Cancer Ther. *14*, 1614–
892 1624.

893 Herbst, R.S., Giaccone, G., de Marinis, F., Reinmuth, N., Vergnenegre, A., Barrios, C.H., Morise, M.,
894 Felip, E., Andric, Z., Geater, S., et al. (2020). Atezolizumab for First-Line Treatment of PD-L1-Selected
895 Patients with NSCLC. N. Engl. J. Med. *383*, 1328–1339.

896 Hidalgo, M., Amant, F., Biankin, A.V., Budinská, E., Byrne, A.T., Caldas, C., Clarke, R.B., de Jong, S.,
897 Jonkers, J., Mælandsmo, G.M., et al. (2014). Patient-derived xenograft models: an emerging platform
898 for translational cancer research. Cancer Discov. *4*, 998–1013.

899 Inda, M.-D.-M., Bonavia, R., and Seoane, J. (2014). Glioblastoma multiforme: a look inside its
900 heterogeneous nature. Cancers *6*, 226–239.

901 Junutula, J.R., Raab, H., Clark, S., Bhakta, S., Leipold, D.D., Weir, S., Chen, Y., Simpson, M., Tsai,
902 S.P., Dennis, M.S., et al. (2008). Site-specific conjugation of a cytotoxic drug to an antibody improves
903 the therapeutic index. Nat. Biotechnol. *26*, 925–932.

904 Junutula, J.R., Flagella, K.M., Graham, R.A., Parsons, K.L., Ha, E., Raab, H., Bhakta, S., Nguyen, T.,
905 Dugger, D.L., Li, G., et al. (2010). Engineered thio-trastuzumab-DM1 conjugate with an improved
906 therapeutic index to target human epidermal growth factor receptor 2-positive breast cancer. Clin.
907 Cancer Res. *16*, 4769–4778.

908 Kim, M., Ma, D.J., Calligaris, D., Zhang, S., Feathers, R.W., Vaubel, R.A., Meaux, I., Mladek, A.C.,
909 Parrish, K.E., Jin, F., et al. (2018). Efficacy of the MDM2 Inhibitor SAR405838 in Glioblastoma Is
910 Limited by Poor Distribution Across the Blood-Brain Barrier. Mol. Cancer Ther. *17*, 1893–1901.

911 Lhospice, F., Brégeon, D., Belmant, C., Dennler, P., Chiotellis, A., Fischer, E., Gauthier, L., Boëdec, A.,
912 Rispaud, H., Savard-Chambard, S., et al. (2015). Site-Specific Conjugation of Monomethyl Auristatin E
913 to Anti-CD30 Antibodies Improves Their Pharmacokinetics and Therapeutic Index in Rodent Models.
914 Mol. Pharm. *12*, 1863–1871.

915   Li, Z., Krippendorff, B.-F., Sharma, S., Walz, A.C., Lavé, T., and Shah, D.K. (2016). Influence of
916   molecular size on tissue distribution of antibody fragments. MAbs *8*, 113–119.

917   Lyon, R.P., Setter, J.R., Bovee, T.D., Doronina, S.O., Hunter, J.H., Anderson, M.E., Balasubramanian,
918   C.L., Duniho, S.M., Leiske, C.I., Li, F., et al. (2014). Self-hydrolyzing maleimides improve the stability
919   and pharmacological properties of antibody-drug conjugates. Nat. Biotechnol. *32*, 1059–1062.

920   Marin, B.-M., Porath, K.A., Jain, S., Kim, M., Conage-Pough, J.E., Oh, J.-H., Miller, C.L., Talele, S.,
921   Kitange, G.J., Tian, S., et al. (2021). Heterogeneous delivery across the blood-brain barrier limits the
922   efficacy of an EGFR-targeting antibody drug conjugate in glioblastoma. Neuro. Oncol.

923   Mullard, A. (2021). FDA approves ADC Therapeutics' loncastuximab tesirine, ushering in a new
924   cytotoxic payload. Nat. Rev. Drug Discov. *10*.

925   Nair, M., Khosla, M., Otani, Y., Yeh, M., Park, F., Shimizu, T., Kang, J.M., Bolyard, C., Yu, J.-G., Kumar
926   Banasavadi-Siddegowda, Y., et al. (2020). Enhancing Antitumor Efficacy of Heavily Vascularized
927   Tumors by RAMBO Virus through Decreased Tumor Endothelial Cell Activation. Cancers *12*.

928   Newman, D.J. (2019). The "Utility" of Highly Toxic Marine-Sourced Compounds. Mar. Drugs *17*, 324.

929   Otani, Y., Yoo, J.Y., Chao, S., Liu, J., Jaime-Ramirez, A.C., Lee, T.J., Hurwitz, B., Yan, Y., Dai, H.,
930   Glorioso, J.C., et al. (2020). Oncolytic HSV-Infected Glioma Cells Activate NOTCH in Adjacent Tumor
931   Cells Sensitizing Tumors to Gamma Secretase Inhibition. Clin. Cancer Res. *26*, 2381–2392.

932   Palmieri, D., Duchnowska, R., Woditschka, S., Hua, E., Qian, Y., Biernat, W., Sosińska-Mielcarek, K.,
933   Gril, B., Stark, A.M., Hewitt, S.M., et al. (2014). Profound prevention of experimental brain metastases
934   of breast cancer by temozolomide in an MGMT-dependent manner. Clin. Cancer Res. *20*, 2727–2739.

935   Parker, N.R., Khong, P., Parkinson, J.F., Howell, V.M., and Wheeler, H.R. (2015). Molecular
936   heterogeneity in glioblastoma: potential clinical implications. Front. Oncol. *5*, 55.

937   Parrish, K.E., Cen, L., Murray, J., Calligaris, D., Kizilbash, S., Mittapalli, R.K., Carlson, B.L., Schroeder,
938   M.A., Sludden, J., Boddy, A.V., et al. (2015). Efficacy of PARP Inhibitor Rucaparib in Orthotopic
939   Glioblastoma Xenografts Is Limited by Ineffective Drug Penetration into the Central Nervous System.
940   Mol. Cancer Ther. *14*, 2735–2743.

941   Phillips, A.C., Boghaert, E.R., Vaidya, K.S., Mitten, M.J., Norvell, S., Falls, H.D., DeVries, P.J., Cheng,
942   D., Meulbroek, J.A., Buchanan, F.G., et al. (2016). ABT-414, an Antibody-Drug Conjugate Targeting a
943   Tumor-Selective EGFR Epitope. Mol. Cancer Ther. *15*, 661–669.

944   Phillips, A.C., Boghaert, E.R., Vaidya, K.S., Falls, H.D., Mitten, M.J., DeVries, P.J., Benatuil, L., Hsieh,
945   C.-M., Meulbroek, J.A., Panchal, S.C., et al. (2018). Characterization of ABBV-221, a Tumor-Selective
946   EGFR-Targeting Antibody Drug Conjugate. Mol. Cancer Ther. *17*, 795–805.

947   Pillow, T.H., Tien, J., Parsons-Reponte, K.L., Bhakta, S., Li, H., Staben, L.R., Li, G., Chuh, J., Fourie-
948   O'Donohue, A., Darwish, M., et al. (2014). Site-specific trastuzumab maytansinoid antibody-drug
949   conjugates with improved therapeutic activity through linker and antibody engineering. J. Med. Chem.
950   *57*, 7890–7899.

951   Rosenthal, M., Curry, R., Reardon, D.A., Rasmussen, E., Upreti, V.V., Damore, M.A., Henary, H.A.,
952   Hill, J.S., and Cloughesy, T. (2019). Safety, tolerability, and pharmacokinetics of anti-EGFRvIII
953   antibody-drug conjugate AMG 595 in patients with recurrent malignant glioma expressing EGFRvIII.
954   Cancer Chemother. Pharmacol. *84*, 327–336.

955 Sarkaria, J.N., Carlson, B.L., Schroeder, M.A., Grogan, P., Brown, P.D., Giannini, C., Ballman, K.V.,
956 Kitange, G.J., Guha, A., Pandita, A., et al. (2006). Use of an orthotopic xenograft model for assessing
957 the effect of epidermal growth factor receptor amplification on glioblastoma radiation response. Clin.
958 Cancer Res. *12*, 2264–2271.

959 Sarkaria, J.N., Hu, L.S., Parney, I.F., Pafundi, D.H., Brinkmann, D.H., Laack, N.N., Giannini, C., Burns,
960 T.C., Kizilbash, S.H., Laramy, J.K., et al. (2018). Is the blood-brain barrier really disrupted in all
961 glioblastomas? A critical assessment of existing clinical data. Neuro. Oncol. *20*, 184–191.

962 Shergalis, A., Bankhead, A., 3rd, Luesakul, U., Muangsin, N., and Neamati, N. (2018). Current
963 Challenges and Opportunities in Treating Glioblastoma. Pharmacol. Rev. *70*, 412–445.

964 Shi, Y., Fan, X., Meng, W., Deng, H., Zhang, N., and An, Z. (2014). Engagement of immune effector
965 cells by trastuzumab induces HER2/ERBB2 downregulation in cancer cells through STAT1 activation.
966 Breast Cancer Res. *16*, R33.

967 Stupp, R., Mason, W.P., van den Bent, M.J., Weller, M., Fisher, B., Taphoorn, M.J.B., Belanger, K.,
968 Brandes, A.A., Marosi, C., Bogdahn, U., et al. (2005). Radiotherapy plus concomitant and adjuvant
969 temozolomide for glioblastoma. N. Engl. J. Med. *352*, 987–996.

970 Stupp, R., Hegi, M.E., Mason, W.P., van den Bent, M.J., Taphoorn, M.J.B., Janzer, R.C., Ludwin, S.K.,
971 Allgeier, A., Fisher, B., Belanger, K., et al. (2009). Effects of radiotherapy with concomitant and
972 adjuvant temozolomide versus radiotherapy alone on survival in glioblastoma in a randomised phase III
973 study: 5-year analysis of the EORTC-NCIC trial. Lancet Oncol. *10*, 459–466.

974 van Tellingen, O., Yetkin-Arik, B., de Gooijer, M.C., Wesseling, P., Wurdinger, T., and de Vries, H.E.
975 (2015). Overcoming the blood-brain tumor barrier for effective glioblastoma treatment. Drug Resist.
976 Updat. *19*, 1–12.

977 Tumey, L.N., Charati, M., He, T., Sousa, E., Ma, D., Han, X., Clark, T., Casavant, J., Loganzo, F.,
978 Barletta, F., et al. (2014). Mild method for succinimide hydrolysis on ADCs: impact on ADC potency,
979 stability, exposure, and efficacy. Bioconjug. Chem. *25*, 1871–1880.

980 Van Den Bent, M., Eoli, M., Sepulveda, J.M., Smits, M., Walenkamp, A., Frenel, J.-S., Franceschi, E.,
981 Clement, P.M., Chinot, O., De Vos, F., et al. (2020). INTELLANCE 2/EORTC 1410 randomized phase II
982 study of Depatux-M alone and with temozolomide vs temozolomide or lomustine in recurrent EGFR
983 amplified glioblastoma. Neuro. Oncol. *22*, 684–693.

984 Weller, M., van den Bent, M., Hopkins, K., Tonn, J.C., Stupp, R., Falini, A., Cohen-Jonathan-Moyal, E.,
985 Frappaz, D., Henriksson, R., Balana, C., et al. (2014). EANO guideline for the diagnosis and treatment
986 of anaplastic gliomas and glioblastoma. The Lancet. Oncology *15*, e395-403.

987 White, J.M., Keinänen, O.M., Cook, B.E., Zeglis, B.M., Gibson, H.M., and Viola, N.T. (2020). Removal
988 of Fc Glycans from [89Zr]Zr-DFO-Anti-CD8 Prevents Peripheral Depletion of CD8+ T Cells. Mol.
989 Pharm. *17*, 2099–2108.

990 Yamazaki, C.M., Yamaguchi, A., Anami, Y., Xiong, W., Otani, Y., Lee, J., Ueno, N.T., Zhang, N., An, Z.,
991 and Tsuchikama, K. (2021). Antibody-drug conjugates with dual payloads for combating breast tumor
992 heterogeneity and drug resistance. Nat. Commun. *12*, 3528.

993 Yonemori, K., Tsuta, K., Ono, M., Shimizu, C., Hirakawa, A., Hasegawa, T., Hatanaka, Y., Narita, Y.,
994 Shibui, S., and Fujiwara, Y. (2010). Disruption of the blood brain barrier by brain metastases of triple-
995 negative and basal-type breast cancer but not HER2/neu-positive breast cancer. Cancer *116*, 302–308.

996 Zhang, Y., Huo, M., Zhou, J., and Xie, S. (2010). PKSolver: An add-in program for pharmacokinetic and
997 pharmacodynamic data analysis in Microsoft Excel. Comput. Methods Programs Biomed. *99*, 306–314.

998 Zimmer, A.S., Van Swearingen, A.E.D., and Anders, C.K. (2020). HER2-positive breast cancer brain
999 metastasis: A new and exciting landscape. Cancer Rep. e1274.

1000